**RESEARCH ARTICLE**

# The effects of axonal beading and undulation on axonal diameter estimation from diffusion MRI: Insights from simulations in human axons segmented from three-dimensional electron microscopy

Hong-Hsi Lee [1,2] | Qiyuan Tian [1,2] | Maxina Sheft [1,3] |
Ricardo Coronado-Leija [4,5] | Gabriel Ramos-Llorden [1,2] | Ali Abdollahzadeh [4,5] |
Els Fieremans [4,5] | Dmitry S. Novikov [4,5] | Susie Y. Huang [1,2]

[1]Athinoula A. Martinos Center for Biomedical Imaging, Department of Radiology, Massachusetts General Hospital, Charlestown, Massachusetts, USA

[2]Harvard Medical School, Boston, Massachusetts, USA

[3]Harvard–MIT Health Sciences and Technology, Cambridge, Massachusetts, USA

[4]Center for Biomedical Imaging, Department of Radiology, New York University School of Medicine, New York, New York, USA

[5]Center for Advanced Imaging Innovation and Research (CAI2R), New York University School of Medicine, New York, New York, USA

**Correspondence**

Hong-Hsi Lee, Athinoula A. Martinos Center for Biomedical Imaging, Department of Radiology, Massachusetts General Hostpial, Charlestown, MA 02129, USA.
Email: HLEE84@mgh.harvard.edu

Qiyuan Tian, Athinoula A. Martinos Center for Biomedical Imaging, Massachusetts General Hostpial, MA 02129, USA.
Email: qiyuantian@mail.tsinghua.edu.cn

**Funding information**

National Institute of Biomedical Imaging and Bioengineering; National Institute of Dental and Craniofacial Research; National Institute of Neurological Disorders and Stroke; National Institute on Aging; NIH Office of the Director

The increasing availability of high-performance gradient systems in human MRI scanners has generated great interest in diffusion microstructural imaging applications such as axonal diameter mapping. Practically, sensitivity to axon diameter in diffusion MRI is attained at strong diffusion weightings $b$, where the deviation from the expected $1/\sqrt{b}$ scaling in white matter yields a finite transverse diffusivity, which is then translated into an axon diameter estimate. While axons are usually modeled as perfectly straight, impermeable cylinders, local variations in diameter (caliber variation or beading) and direction (undulation) are known to influence axonal diameter estimates and have been observed in microscopy data of human axons. In this study, we performed Monte Carlo simulations of diffusion in axons reconstructed from three-dimensional electron microscopy of a human temporal lobe specimen using simulated sequence parameters matched to the maximal gradient strength of the next-generation Connectome 2.0 human MRI scanner ($\lesssim 500\,\text{mT/m}$). We show that axon diameter estimation is accurate for nonbeaded, nonundulating fibers; however, in fibers with caliber variations and undulations, the axon diameter is heavily underestimated due to caliber variations, and this effect overshadows the known overestimation of the axon diameter due to undulations. This unexpected underestimation may originate from variations in the coarse-grained axial diffusivity due to caliber variations. Given that increased axonal beading and undulations have been observed in pathological tissues, such as traumatic brain injury and ischemia, the interpretation of axon diameter alterations in pathology may be significantly confounded.

**KEYWORDS**
axonal diameter mapping, axonal undulation, caliber variation, diffusion MRI, Monte Carlo simulation, spherical mean signal

---

# 1 | INTRODUCTION

Diffusion MRI (dMRI) probes tissue microstructure at the mesoscopic scale and enables estimation of cellular-level features such as axon diameter and cellular size.[1] Identifying alterations in axon diameter in white matter offers the enticing possibility of characterizing tissue pathology in the living human brain in conditions such as multiple sclerosis[2–5] and amyotrophic lateral sclerosis.[6,7] This signal sensitivity to the axon diameter, further weighted by the axon volume, gives a strong preference to the tail of the axon diameter distribution,[8,9] providing the interpretation of axonal diameter mapping (ADM) results in the brain using dMRI with strong gradients.[4,5,9–16]

In healthy white matter, ADM is confounded by a number of known factors: non-Gaussian (time-dependent) diffusion in extra-axonal space, relevant at low-to-moderate diffusion weightings, both transverse[8,17,18] and along axons[17,19,20]; and orientation dispersion,[9,14] observed even in highly aligned fiber regions such as the corpus callosum[21,22] and spinal cord.[23,24] In addition, intercompartmental water exchange between the intra- and extra-axonal space is assumed to be slow and negligible at clinical diffusion times.[25,26] To reduce the confound from the extra-axonal space, one can apply sufficiently strong diffusion weighting to suppress the extra-axonal signal.[9] To factor out the fiber orientation dispersion, diffusion signals are directionally averaged—known as powder-averaging[27] or the spherical mean technique (SMT)[28]—for each diffusion weighting $b$, and the deviation from the $1/\sqrt{b}$ scaling at high $b$ yields an estimate of axon diameter.[9,14]

Complex noncylindrical axonal shapes can be broken down into two components: *caliber variations* (beading), on the scale of a few microns,[29] and *axonal undulations* (changes in local axon direction), with wavelengths of a few tens of microns.[30] For the application of diffusion gradients *perpendicular to a highly aligned* fiber bundle, the impact of realistic geometries on ADM has been studied: Budde and Frank[29] performed diffusion simulations in beaded cylinders and showed that beading led to increased radial diffusivity, which can be interpreted as overestimated axon diameter[31,32]; Nilsson et al[30] and Brabec et al[33] performed diffusion simulations in undulating thin fibers and cylinders, showing that undulations led to overestimated axon diameter. These studies demonstrated potential confounds in ADM models applied to complex axonal geometries, particularly when such models were fitted to diffusion signals perpendicular to a single fiber bundle.[4,5,10] However, these models may not be optimal for estimation of axon diameter in the brain, where more than 60% of MR voxels have crossing fibers[34] with nontrivial fiber dispersion.

To factor out the fiber orientation dispersion, the ADM model using SMT was first tested in mouse brain axons extracted from three-dimensional EM,[35] where ADM is only accurate for straight axons at shorter time scales $\delta < 10$ ms. At longer time scales, the axon diameter is *underestimated*. This was an unexpected finding, since, conventionally, both caliber variations and undulation are known confounds that lead to overestimated axon diameter. Similarly, the SMT-based ADM model was validated in vervet monkey brain axons reconstructed from X-ray nanoholotomography,[36] in which an underestimation of axon diameter was also observed in axons with diameters smaller than 3 microns. The interpretation of this finding was unclear. To identify the cause of this surprising bias, it is necessary to separate and quantify the effect of caliber variations and undulation on ADM. Here, we provide additional insights by studying realistic tissue substrates derived from human brain axons and performing simulations in artificially generated fibers that mimic the realistic axons by tuning the caliber variations and undulations.

In this work, we make use of a 1.4-petabyte EM volume of human temporal lobe tissue and the adjacent subcortical white matter that was recently made publicly available.[37] This dataset serves as a valuable resource for building numerical phantoms for the characterization and validation of ADM in human brain white matter. We segment 76 myelinated axons (33.5–189.3 $\mu$m in length, Figure 1) in subcortical white matter of this human brain EM sample using U-Nets[38] and generate undulating, beaded fibers of circular cross-sections with tuned caliber variations and undulations (Figure 2a) similar to those observed in real axons in EM. We then calculate intra-axonal diffusion signals using Monte Carlo (MC) simulations of diffusion in segmented axons and artificial fibers. The diffusion signals are calculated based on a diffusion MR protocol on the latest human Connectome 2.0 scanner with gradient strength $\lesssim 500$ mT/m.[39] For fibers of the same scaling of caliber variations and undulations, we generate intra-axonal diffusion signals by taking their volume-weighted sum. Diffusion in the extra-axonal space and cerebrospinal fluid (CSF) is approximated by anisotropic or isotropic Gaussian diffusion, but is generally inessential, as we perform parameter estimation at high $b$. To reveal the effect of axonal features on axonal diameter mapping using spherical mean signals, we test ADM models in (i) a single-compartment model with only intracellular signal and (ii) a multiple-compartment model with intra- and extracellular spaces and a CSF component. MC simulations in both cases show that caliber variations and undulations result in under- and overestimation of the axon diameter, respectively.

# 2 | METHODS

All the data are publicly available in the literature[37] following the ethical standards of Harvard University. This article does not contain any studies with human participants and animals performed by any of the authors.
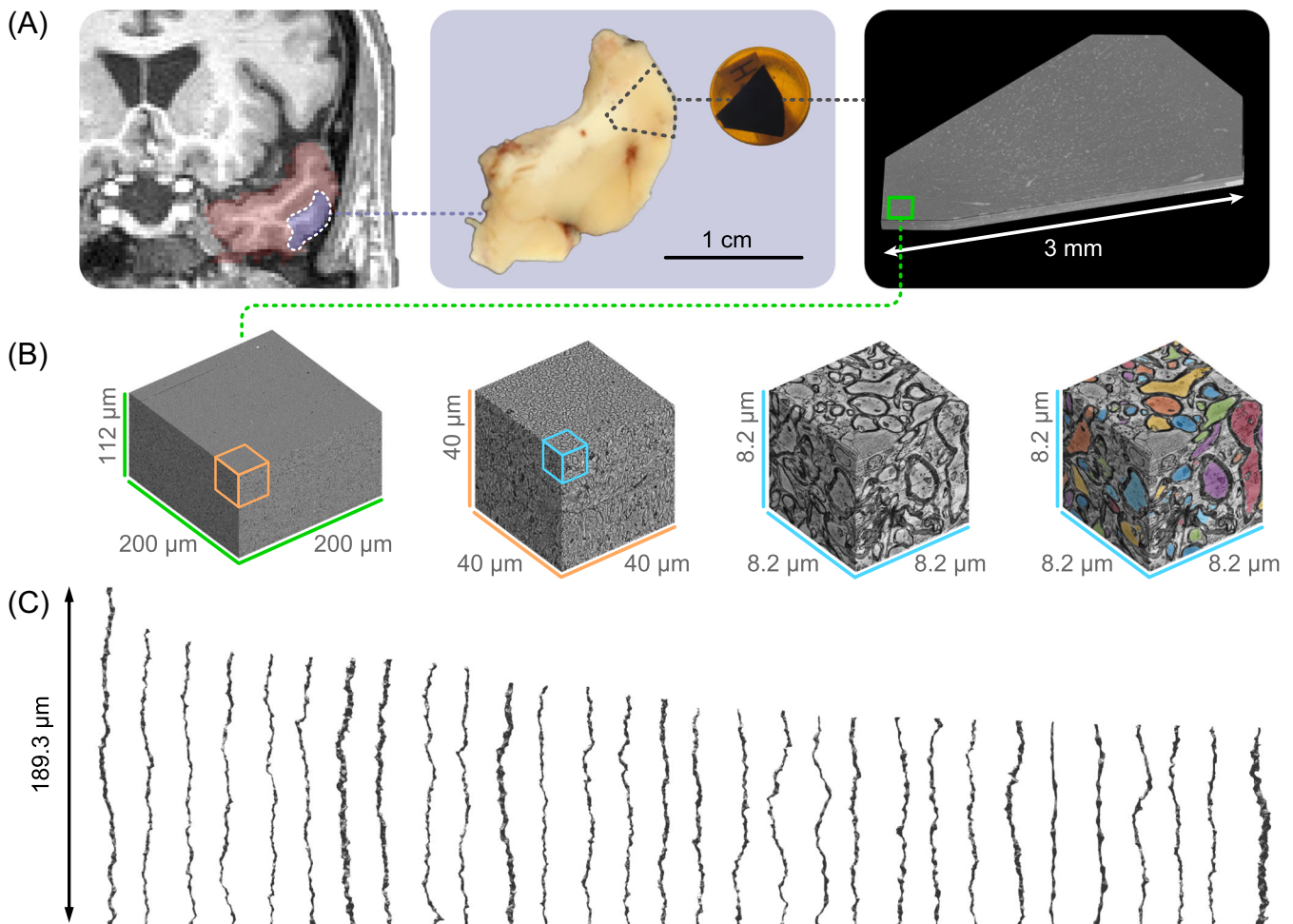
**FIGURE 1** (a) Non-lesional brain tissue (purple) was obtained from the left middle temporal gyrus (red) of a 45-year-old female undergoing surgery for hippocampal sclerosis, drop-fixed in glutaraldehyde/paraformaldehyde fixative, stained with osmium tetroxide, and embedded in resin.[37] The tissue was subsequently scanned with a high-resolution multibeam scanning electron microscope. (b) The $200 \times 200 \times 112\ \mu m^3$ subset of the EM volume corresponding to subcortical white matter (green rectangle in the right part of panel a) was segmented using 2d and 3d U-Nets. (c) The segmented intra-axonal space of myelinated axons longer than $33.5\ \mu m$ was aligned along the z-axis, resulting in 76 axons ranging from $33.5–189.3\ \mu m$ long. Panel (a) is adapted from Shapson-Coe et al[37] with permission from bioRxiv.

## 2.1 | Human brain EM segmentation

Non-lesional brain tissue was obtained from the anterior portion of the left middle temporal gyrus of a 45-year-old female during surgery for re-section of an epileptogenic focus in the left hippocampus[37] (Figure 1a). The pathological evaluation showed hippocampal sclerosis, whereas the brain tissue sampled from the anterior portion of the middle temporal gyrus showed no diagnostic abnormality recognized. The tissue sample was fixed by immersion in cold 2.5% paraformaldehyde / 2.5% glutaraldehyde in 0.1 M sodium cacodylate buffer (pH 7.4) and maintained in fixative overnight. It was then washed in 0.1 M sodium cacodylate and 2 mM $CaCl_2$ buffer and trimmed to $2 \times 3 \times 0.2\ mm^3$ and scanned with a multibeam serial-section scanning electron microscope (Sigma, Carl Zeiss) using $4 \times 4\ nm^2$ pixels and 33-nm slice thickness. The $200 \times 200 \times 112\ \mu m^3$ subset of subcortical white matter was downsampled to $32 \times 32\ nm^2$ pixels and 33-nm slice thickness and segmented using 2d and 3d U-Nets[38] (Figure 1b), initially trained on ground-truth segmentation of myelin and intra-axonal space in EM images of mouse corpus callosum.[22] The voxel size was further downsampled to $64 \times 64 \times 64\ nm^3$ after segmentation. The segmented intra-axonal spaces of myelinated axons longer than $33.5\ \mu m$ were aligned along the z-axis, resulting in 76 axons ranging from $33.5–189.3\ \mu m$ long (Figure 1c).
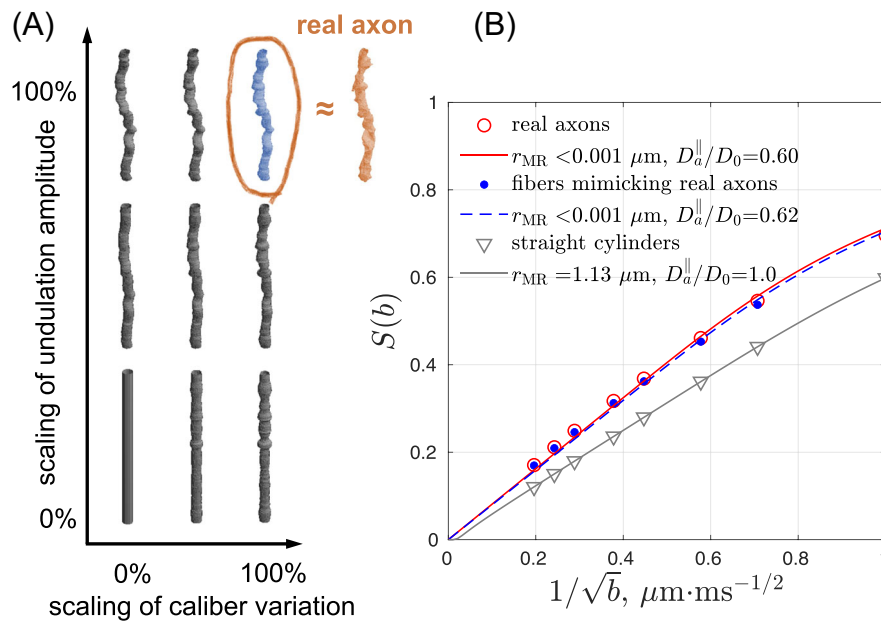
**FIGURE 2** To mimic axonal geometries based on their most relevant features, we created (a) fibers of circular cross-sections (blue) with the same undulations and caliber variations as real axons (red), and fibers of circular cross-sections (gray) with undulation amplitudes $w_0$ and coefficients of variation of radius CV(r) scaled from 0% to 100%. (b) The simulated spherical mean signals in real axons (Figure 1c) and axon-mimicking fibers (panel a, blue) were consistent, and their MR-estimated axon radii < 0.001 $\mu$m were much smaller than the histological ground truth 1.1 $\mu$m in Figure 4a. In addition, the simulated signals in real axons are very different from the simulated signals in nonbeaded, nonundulating straight cylinders of the same length and volume (gray data point). The straight cylinders have an MR-estimated axon radius = 1.13 $\mu$m, consistent with the histology.

## 2.2 | Axon morphology analysis

The inner axonal radius along individual axons was estimated by using the equivalent circle radius $r$, defined as the radius of an equivalent circle with the same cross-sectional area as the intra-axonal space.[22,35,40,41] The caliber variation of individual axons was defined as the coefficient of variation of the radius[22,35]

$$\mathrm{CV}(r) \equiv \mathrm{std}(r)/\langle r \rangle.$$

The axon radius estimated by MR is heavily weighted by thick axons.[8,31] Diffusion weighting, introduced by applying magnetic field gradients, leads to spatial variations of the Larmor frequency across an axon cross-section. For the practically relevant case of wide-pulsed gradients, when gradient duration $\delta$ exceeds the time to diffuse across axon radius $r$, signal attenuation can be interpreted as transverse relaxation,[18] $-\ln S \sim R_2^* \cdot 2\delta$, occurring during the net pulse duration $2\delta$, with a rate $R_2^* \propto r^4$ that is strongly sensitive to the radius.[31,32] This signal sensitivity is further weighted by the axon volume $\propto r^2$, leading to the effective MR axon radius $r_{\mathrm{eff}}$ calculated based on the equivalent circle radius $r$[8,9,35,42]:

$$r_{\mathrm{eff}} = \left( \frac{\langle r^6 \rangle}{\langle r^2 \rangle} \right)^{1/4}. \tag{1}$$

This is the histological reference to be compared with ADM results.

To quantify axonal undulations, the axonal skeleton was built by connecting the center of mass of each intra-axonal cross-section along individual axons. The undulation amplitude $w_0$ and wavelength $\lambda$ were calculated using a simplified single harmonic model for the axonal skeleton.[35,43]

## 2.3 | Undulating, beaded fibers similar to actual axons

To mimic axonal geometries based on their most relevant features and understand the impact of these features on axonal diameter mapping, we created artificial fibers of circular cross-sections with similar undulations and caliber variations to realistic axons.[20]

To begin with, we calculated the skeleton of a realistic axon, aligned the axon and its skeleton to the $z$-axis, and centered it at the origin, yielding a skeleton coordinate $(s_x, s_y, z)$. The skeleton's deviation from the $z$-axis, that is, $(s_x, s_y)$, was scaled by a scaling factor $p_w$ of undulation amplitude from $p_w = 0\%$ (straight fiber), 25%, 50%, 75%, and 100% (the same undulations as realistic axons). The undulation amplitude $w_0$ was scaled by $p_w$ due to $w_0^2 = s_x^2 + s_y^2$. After generating the fiber skeleton, we convolved a spherical kernel with the skeleton to generate the fiber shape for simulations. The radius $r$ of the spherical kernel varies along the skeleton. To retrieve the radius variation from the realistic axon, we calculated the equivalent circle radius $r(z)$ of each axonal cross-section at $z$. The equivalent circle radius of the axonal cross-section was defined as the radius of an equivalent circle with the same cross-sectional area.[22,40,41] The coefficient of variation of the radius, $CV[r(z)]$, is scaled by a scaling factor $p_r$ of caliber variation from $p_r = 0\%$ (no caliber variations), 25%, 50%, 75%, and 100% (the same caliber variations as realistic axons). The undulation wavelength $\lambda$ and the volume of each artificial fiber were kept the same as for the realistic axon.

The artificial fibers with $(p_w, p_r) = (100\%, 100\%)$ had similar shapes to realistic axons, and yet their cross-sections were always circular. The scaling of fiber shapes was never beyond the EM-segmented axons, for which the scalings of $w_0$ and $CV(r)$ were defined as 100% and considered as "strong" ones. The ex vivo human axons have very strong undulations and caliber variations, potentially due to immersion fixation, and thus we choose not to create fibers with these features larger than the observed values in EM. For each realistic axon, we generated (5 $p_w$) $\times$(5 $p_r$) = 25 artificial fibers; for 76 axons, we created 25 $\times$76 = 1900 artificial fibers and performed simulations using these fibers.

## 2.4 | Monte Carlo (MC) simulations

MC simulations were implemented in CUDA C++ for diffusion in the three-dimensional microgeometry of intra-axonal space from the selected 76 axons and their fiber derivatives were aligned in the $z$-direction. The cell shapes were described by voxelized geometries based on the voxel size $(64 \text{ nm})^3$ of EM segmentation. 100,000 random walkers per fiber were employed, diffusing for $1.1\times10^5$ steps with a duration of $2.8\times10^{-4}$ ms and a step length of 58 nm for each step.[20,35,43,44] The intrinsic diffusivity was set to $D_0 = 2\,\mu\text{m}^2/\text{ms}$.[45–48] To prevent restriction at the two ends of the axonal geometries, the top and bottom faces of each fiber were extended by reflective copies using mirroring boundary conditions. In other words, random walkers were blocked and reflected back to the domain, and yet their diffusion displacements were calculated as if they diffused in the extended reflective copies with respective to the top and bottom faces. The diffusion signal resulting from a pulsed-gradient spin-echo sequence was calculated, with pulse duration $\delta = 10$ ms, interpulse interval $\Delta = 20$ ms, eight $b$ values $b = [1, 2, 3, 5, 7, 12, 17, 26]$ ms/$\mu$m$^2$ with maximal gradient strength $G_{\max} = 470$ mT/m, and 60 gradient directions per $b$ shell. The MC simulations took 10 days on an NVIDIA V100 GPU core. Here we aimed to test the Connectome 2.0 scanner protocol ($G_{\max} = 500$ mT/m) for potential applications of ADM on our latest human scanner.

The normalized simulated signal of the $i$th axon in gradient direction $\hat{g}$ was denoted as $\tilde{S}_{a,i}(b, \hat{g})$, with the tilde indicating the signal derived from MC simulations. The normalized spherical mean signal $\tilde{S}_{a,i}(b)$ of the $i$th axon was calculated by averaging diffusion-weighted signals $\tilde{S}_{a,i}(b, \hat{g})$ in 60 directions over each $b$ shell.

To demonstrate the accuracy of the above standard simulation protocol, we performed an additional simulation in a real axon of the largest volume with a more stringent simulation setup. We applied more random walkers $(10^6)$ in the axon with a shorter length (32 nm) for each step. Simulation results showed that the simulated spherical mean signal of the two protocols differed by only 0.2% of the diffusion signal at the highest $b$ value (Supplementary Figure S1).

## 2.5 | Signal generation

To demonstrate the effect of axonal shape on diameter mapping, we generated normalized spherical mean signals in one compartment (i.e., intra-axonal space) or multiple compartments (i.e., intra-axonal space, extra-axonal space, and CSF). In this study, all diffusion signals $S$ were normalized such that the non diffusion-weighted signal $S_0 \equiv 1$.

### 2.5.1 | Spherical mean signal in one compartment

The intra-axonal signal $\tilde{S}_a(b)$ was created by randomly choosing 38 out of 76 axon fiber derivatives, with the same scaling factor combination of undulations and caliber variations, $(p_w, p_r)$ in Section 2.3, over 500 different realizations for bootstrapping and calculating the volume-weighted sum of their simulated spherical mean signals $\tilde{S}_{a,i}(b)$:

$$S(b) = \tilde{S}_a(b) = \sum_{i \in \Omega} f_i \cdot \tilde{S}_{a,i}(b), \tag{2}$$

where $\Omega$ is a list of the chosen axons in each iteration and $f_i$ is the volume fraction of the $i$th fiber in the list $\Omega$, such that $\sum_{i \in \Omega} f_i = 1$. For each combination of scaling factors $(p_w, p_r)$, we calculated (i) the difference of the ground-truth value of axon radius in histology $r_{eff}$ and the model fitting result $r_{MR}$ in simulated signals (Section 2.6.1) and (ii) the normalized root-mean-square error (NRMSE) between the histology and simulations over 500 different realizations of bootstrapping to evaluate the bias in axon diameter mapping due to realistic axonal shape features (Section 2.7).

Here we used the bootstrapping due to the small sample size (76 axons) and unknown underlying axonal shape distribution over whole brain white matter.

## 2.5.2 | Spherical mean signal in multiple compartments

To create signals similar to those in white matter, we combined signals in two additional compartments (extra-axonal space and CSF) with the simulated spherical mean signal $\tilde{S}_a$ in intra-axonal space in Section 2.5.1:

$$S(b) = (1 - f_{csf}) \cdot \left( f_a \tilde{S}_a + (1 - f_a) S_e \right) + f_{csf} \cdot S_{csf}, \tag{3}$$

where $f_a$ and $f_{csf}$ are the relaxation-weighted volume fractions of the intra-axonal space and CSF. $S_e$ and $S_{csf}$ are the normalized spherical mean signals in the extra-axonal space and CSF, where diffusion is modeled as axisymmetric Gaussian ellipsoids and free diffusion, respectively[14,27,28,49]:

$$S_e(b) = \exp(-b D_e^{\perp}) \cdot h\left( b(D_e^{\parallel} - D_e^{\perp}) \right), \tag{4}$$

$$S_{csf}(b) = \exp(-b D_{csf}), \tag{5}$$

where

$$h(x) = \int_0^1 d\zeta \, e^{-x\zeta^2} = \sqrt{\frac{\pi}{4}} \cdot \frac{\mathrm{erf}(\sqrt{x})}{\sqrt{x}}, \tag{6}$$

where $\mathrm{erf}(\cdot)$ is the error function, $D_e^{\parallel}$ and $D_e^{\perp}$ are the extra-axonal diffusivities along and transverse to the axonal segments, respectively, and the CSF diffusivity $D_{csf}$ was fixed at $3 \, \mu m^2/ms$. The simulated intra-axonal signal $\tilde{S}_a$ in each bootstrapping iteration was combined with the extra-axonal space and CSF signals, and the value of each parameter was randomly chosen in the range $f_a \in [0.5, 1]$, $f_{csf} \in [0, 0.2]$, $D_e^{\parallel} = 2 \, \mu m^2/ms$, and $D_e^{\perp} \in [0.5, 1.5] \, \mu m^2/ms$.

We note that signal (3) with the extra-axonal contribution (4) assumes Gaussian extra-axonal diffusion within each fiber fascicle and neglects the time-dependent diffusion effects[8] that can bias ADM further at low $b$. Hence, its applicability is skewed towards large $b$, where $S_e \ll 1$ is negligible.

## 2.6 | Axonal diameter mapping

Axon diameter estimation using the spherical mean signals factors out fiber dispersion and simplifies the functional form in model fitting. Here we compared two approaches to performing axonal diameter mapping using the spherical mean signal (Figure 3). The first approach used the single-compartment SMT model for intra-axonal signals. The second approach used the multicompartmental AxCaliber-SMT model for the combined signals of intra-axonal, extra-axonal, and CSF signals.

## 2.6.1 | Single-compartment SMT, Figure 3a

Approximating real axons as a collection of cylindrical segments of length $L_d \sim (D_a^{\parallel} t)^{1/2}$ at diffusion time $t$, the normalized spherical mean signal of the intra-axonal space is given by[9,14,27,28,47,49]

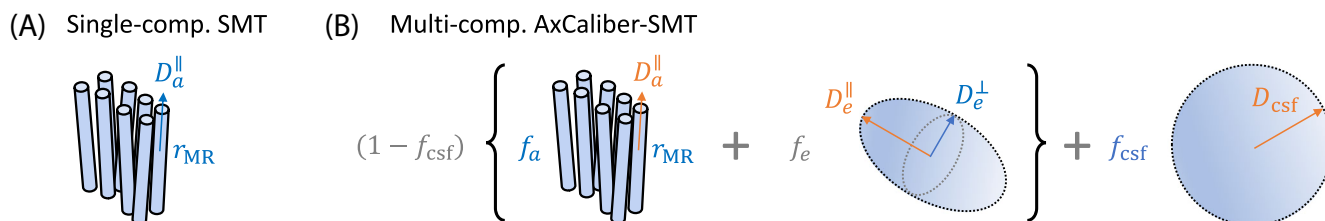$$S(b) = S_a(b) = \exp(-b D_a^{\perp}) \cdot h(A_a), \tag{7}$$

**FIGURE 3** Biophysical modeling of the diffusion MRI signal for axonal diameter mapping. (a) Single-compartment SMT (Section 2.6.1) only includes the spherical mean of the intra-axonal signal in Equation (7). We fit this model to the spherical mean MC-simulated signals of the intra-axonal space (Section 2.5.1). (b) Multicompartmental AxCaliber-SMT (Section 2.6.2) includes the spherical mean of the intra-axonal space, extra-axonal space, and CSF signals in Equation (10). We fit this model to the generated spherical mean signals of the intra-axonal space, extra-axonal space, and CSF (Section 2.5.2). In each model, estimated parameters are in blue, fixed parameters are in orange, and the dependent parameters are in gray, e.g., extra-axonal volume fraction $f_e = 1 - f_a$

where $h(x)$ is defined in Equation (6),

$$A_a = b(D_a^{\parallel} - D_a^{\perp}) \simeq bD_a^{\parallel}, D_a^{\parallel} \gg D_a^{\perp}, \tag{8}$$

and $D_a^{\parallel}$ and $D_a^{\perp}$ are the intra-axonal diffusivities along and transverse to the axonal segments, respectively. An axon radius of $1\,\mu m$ yields an estimate of $D_a^{\perp} \sim 4.44 \times 10^{-4} \mu m^2/ms$[31] with $D_0 = 2\,\mu m^2/ms$ at $\delta = 10\,ms$ and $\Delta = 20\,ms$. In other words, $D_a^{\perp}$ is smaller than $D_a^{\parallel}$ by three orders of magnitude, justifying the approximation in Equation (8). This model is fitted to the spherical mean signal of the intra-axonal space generated by the MC simulations (Equation 2) using nonlinear least squares with positive constraints for all parameters. This is a two-parameter fit with parameters $D_a^{\parallel}$ and $D_a^{\perp}$.

The estimated $D_a^{\perp}$ is translated into the MR-estimated axon radius in Neuman's limit[9,31]:

$$r_{MR} = \left(\frac{48}{7}\delta\left(\Delta - \frac{\delta}{3}\right)D_0 D_a^{\perp}\right)^{1/4}, \tag{9}$$

with intrinsic diffusivity $D_0$ fixed at $2\,\mu m^2/ms$, matching the value in simulations. Equation (9) is applicable in the wide pulse limit, that is, $\delta \gg r^2/D_0$.[31,32] Given that the effective axon radius is about $1\,\mu m$ in histology (dominated by the tail of the axon radius distribution, Equation (1) and Figure 4a), the pulse width $\delta = 10\,ms$ is indeed much longer than the correlation time $r^2/D_0 \sim 0.5\,ms$.

To evaluate the performance of axonal diameter mapping with and without noise, we fit the single-compartment model in Equation (7) to the noiseless signal $\tilde{S}_a(b)$ in Section 2.5.1 and its magnitude signal with Rician noise added, where the noise levels in the real and imaginary parts of the signal are both $\sigma = S_0/SNR$[50,51] with non diffusion-weighted signal $S_0 \equiv 1$ and $SNR = \infty$ (no noise) or 100, respectively.

## 2.6.2 | Multicompartmental AxCaliber-SMT, Figure 3b

To describe multiple compartments in white matter for both low and high $b$, we model the spherical mean signal as consisting of contributions from the intra-axonal space, extra-axonal space, and CSF[14,28]:

$$S(b) = (1 - f_{csf}) \cdot (f_a S_a + (1 - f_a)S_e) + f_{csf} \cdot S_{csf}, \tag{10}$$

where $S_a$, $S_e$, and $S_{csf}$ are the spherical mean signals described in Equations (7), (4), and (5), and time-dependent diffusion effects in the extra-axonal space are neglected. This is a six-parameter fit with parameters $(f_a, f_{csf}, D_a^{\parallel}, D_a^{\perp}, D_e^{\parallel}, D_e^{\perp})$, and $D_{csf}$ fixed to $3\,\mu m^2/ms$. It is difficult to fit six parameters reliably due to the parameter degeneracy problem,[46,52] and thus $D_a^{\parallel} = D_e^{\parallel}$ were both fixed at 1.2, 1.7, or $2\,\mu m^2/ms$ to stabilize the fitting, leading to a four-parameter fit. The axon radius $r_{MR}$ is again estimated based on $D_a^{\perp}$ in Neuman's limit in Equation (9).

To evaluate the ADM performance, we fit the multicompartmental model in Equation (10) to the combined signal in Equation (3) using nonlinear least squares with positive constraints for all parameters. The magnitude signals are composed of MC-simulated signals in intra-axonal space and added signals in the extra-axonal space and CSF with and without Rician noise, where the noise levels in the real and imaginary parts are both $\sigma = S_0/SNR$ with $S_0 \equiv 1$ and $SNR = \infty$ (no noise) and 100, respectively.
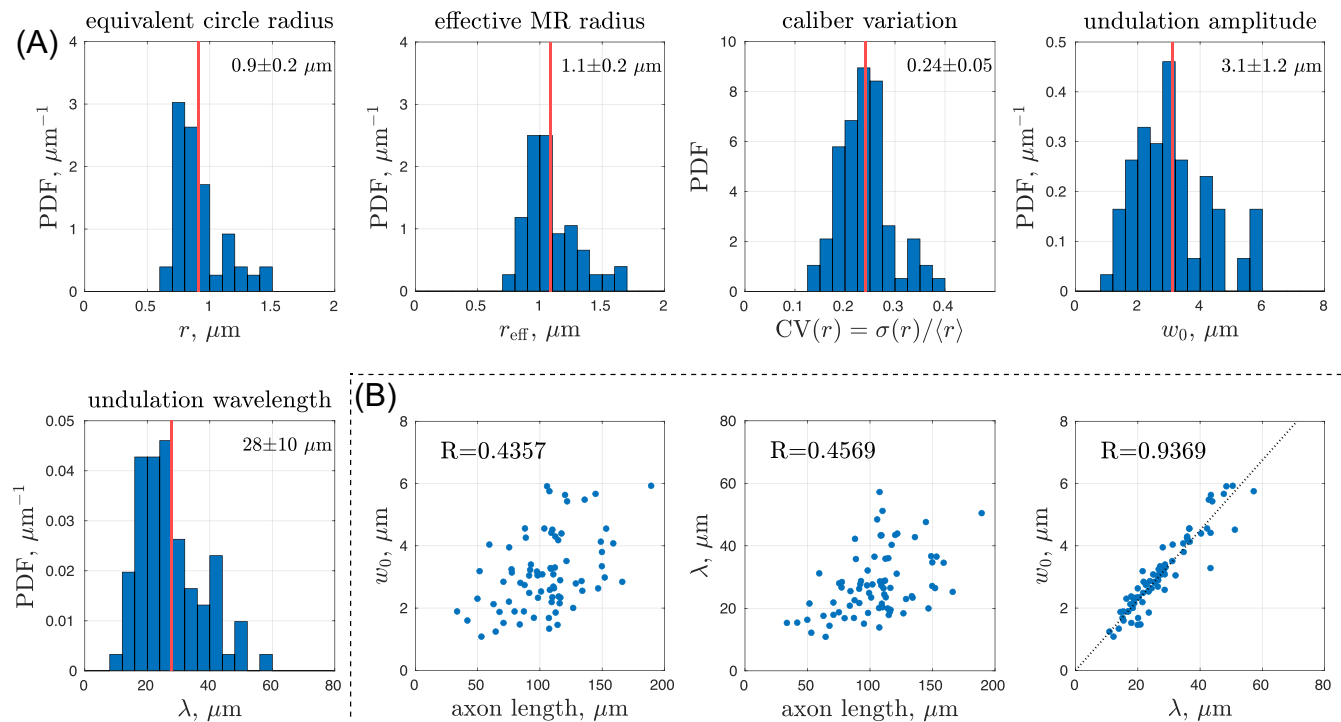
**FIGURE 4** Features of myelinated axons in the human white matter sample. (a) Effective MR axon radius $r_{\text{eff}}$ and caliber variation CV($r$) were calculated based on the equivalent circle radius $r$, and undulation amplitude $w_0$ and wavelength $\lambda$ were calculated using a simplified single harmonic model for axonal skeletons. The mean (red line) and standard deviation were reported. (b) Undulation amplitude and wavelength were highly correlated, and both showed much lower correlations with axon length.

## 2.7 | Comparison of estimated axonal radii with histology

To evaluate the accuracy and precision of the model fitting, we compared the MR-estimated axon radius $r_{\text{MR}}$ in Equation (9) with the histological reference $r_{\text{eff}}$ in Equation (1). We calculated their offset and the NRMSE, which is defined as the ratio of the RMSE to the reference's mean value. Similarly, for additional parameters in the multicompartmental AxCaliber-SMT model, we calculated the offset and NRMSE of the estimated parameters ($f_a$, $f_{\text{csf}}$, $D_e^\perp$) and the values used for signal generation, which served as the ground truth.

## 2.8 | Radial diffusivity and axial diffusivity inside an axon

The radial diffusivity $D_a^\perp$ and axial diffusivity $D_a^\parallel$ inside an axon in Equation (7) are related to both undulations[30,33,35] and caliber variations.[8,20,35] In the narrow pulse limit, the gradient pulse width is so short that the spin does not have time to diffuse across the cell geometry, and the functional forms of diffusivity are given by the mean-squared displacement snapshotted by the diffusion gradient pair. However, limited by the maximal gradient strength and slew rate, diffusion measured in the brain tissue is usually in the wide pulse regime, where each spin explores sufficiently across the cell geometry during each gradient pulse. In this so-called *motional narrowing* phenomenon, all spins have similar phase distributions. Considering the second order of the diffusional phase, the functional form of diffusivity can be calculated by using a Gaussian phase approximation. Here we elaborate the diffusivity of a wide pulse along and transverse to a fiber and correlate the theoretical prediction with the fitted parameters inside axons.

### 2.8.1 | Radial diffusivity and its correlation with undulations and caliber variations

In the wide pulse limit, such that $\delta \gg r^2/D_0$, the spin inside a fiber explores the cross-section of radius $r$ sufficiently during the pulse width $\delta$. In this case, the radial diffusivity inside a straight fiber with caliber variations is given by[8,31,32,35]

$$D_{\text{bead}}^{\perp} \simeq \frac{7}{48} \frac{r_{\text{eff}}^4}{D_0} \frac{1}{\delta(\Delta - \delta/3)}, \tag{11}$$

where the subscript "bead" denotes the caliber variation (beading) and the effective radius $r_{\text{eff}}$ is in Equation (1). This is where the definition (9) of MR-estimated axon radius $r_{\text{MR}}$ originally comes from. However, the radial diffusivity inside a fiber can be confounded by undulations. Considering an undulating thin fiber without caliber variations, its wide pulse diffusivity can be approximated by using a simplified single-harmonic fiber model[35]:

$$D_u^{\perp} \simeq \frac{w_0^2 t_u^2}{4\delta^2(\Delta - \delta/3)} \cdot \left[2\frac{\delta}{t_u} - 2 + 2e^{-\Delta/t_u} + 2e^{-\delta/t_u} - e^{-(\Delta-\delta)/t_u} - e^{-(\Delta+\delta)/t_u}\right], \tag{12}$$

where $w_0$ is the undulation amplitude and $t_u = \lambda^2/(4\pi^2 D_a^{\parallel})$ is the correlation time corresponding to the undulation wavelength $\lambda$. We expect to observe an overestimated axon radius due to this additional contribution of radial diffusivity due to undulations.

## 2.9 | Axial diffusivity and its correlation with undulations and caliber variations

The measurement of axial diffusivity along axons is usually confounded by the fiber dispersion. Instead, estimating axial diffusivity $D_a^{\parallel}$ based on the spherical mean signal effectively factors out the effect of dispersion, revealing the actual value of axial diffusivity and its correlation with undulations and caliber variations. However, the estimated axial diffusivity in axonal diameter mapping is an average along axonal segments (of length $\sim (D_a^{\parallel} t)^{1/2}$) that may orient in slightly different directions due to undulations. The estimated axial diffusivity is not exactly the same as the axial diffusivity projected along the axon's main axis. Further, the bias in axon diameter estimation can lead to bias in estimated axial diffusivity. Therefore, without the consideration of higher order effects (time dependence), we only correlate the estimated axial diffusivity in axonal diameter mapping with the theoretical predictions due to undulations and caliber variations in the long time limit ($t \rightarrow \infty$), respectively. In Appendices A and B, we introduce the full functional form of axial diffusivity time dependence due to undulations and caliber variations for completeness.

### 2.9.1 | The impact of undulations on axial diffusivity

To investigate the effect of undulations on axial diffusivity, we evaluate the diffusivity along a simplified single-harmonic, undulating fiber with no caliber variations. In the long time $t \rightarrow \infty$ limit, the axial diffusivity in an undulating thin fiber is given by[35]

$$D_{\infty,u} \simeq D_0 \left(1 - \frac{2\pi^2 w_0^2}{\lambda^2}\right), \frac{w_0}{\lambda} \ll 1. \tag{13}$$

The approximation of small undulation is justified by the small value $w_0/\lambda \approx 0.11$ in real human axons (Figure 4).

### 2.9.2 | The impact of caliber variations on axial diffusivity

Diffusion along neurites in brain gray matter and white matter is restricted by caliber variations (beading), spines, shafts, branching, and other microstructural inhomogeneity,[20,53–56] the long-range fluctuations of which are characterized by Poisson statistics and a structural exponent $p = 0$ in the power spectrum along neurites. At clinical diffusion times, diffusion in three-dimensional neurite structures effectively degenerates to one-dimensional diffusion along neurites due to the coarse-graining over diffusion lengths longer than the typical length scales captured by cellular-level restrictions and axon caliber.[17,19,20,57,58] Recently, Abdollahzadeh et al[59] considered narrow axons with varying cross-sections $A(z)$ along a length $z$ of axon skeleton and derived the exact relation between the cell geometry and diffusion properties based on the Fick–Jacob equation; in the long time $t \rightarrow \infty$ limit, the axial diffusivity $D_{\infty,\text{bead}}$ in a straight fiber with caliber variation is given by

$$\frac{D_0}{D_{\infty,\text{bead}}} = \left\langle \frac{\bar{A}}{A(z)} \right\rangle, \tag{14}$$

with $\bar{A}$ the mean cross-sectional area. Assuming that the variation of cross-sectional area is small, such that $|\delta A(z)| \ll \bar{A}$, where $\delta A(z) = A(z) - \bar{A}$, the above solution can be approximated by

$$\frac{D_0}{D_{\infty,\text{bead}}} \simeq 1 + \frac{\langle \delta A^2 \rangle}{\bar{A}^2} \simeq 1 + 4 \cdot \text{CV}^2(r), \tag{15}$$

as observed earlier in Lee et al.[20] Here we use the relation $\delta A \simeq 2\pi \bar{r} \delta r$, $\bar{A} \simeq \pi \bar{r}^2$, and $\text{CV}(r) = \langle \delta r^2 \rangle / \bar{r}^2$ with mean radius $\bar{r}$ and radius variation $\delta r = r(z) - \bar{r}$ to simplify the equation.

### 2.9.3 | Correlation of fitted axial diffusivity to predictions

To correlate the fitted axial diffusivity $D_a^{\parallel}$ in ADM with the above theory, we compared the fitted $D_a^{\parallel}$ values (obtained by fitting Equation 7 to simulated intra-axonal signals) with the theoretical prediction due to undulations (13) and caliber variations (14). We calculated the Pearson correlation coefficient of the 500 different realizations of bootstrapping for the signal generation in Section 2.5.1.

## 2.10 | Data and code availability

The EM data can be downloaded on Neuroglancer.[37] The simulation codes can be downloaded on the Github page.

## 3 | RESULTS

### 3.1 | Histology analysis

In this human brain EM sample, we segmented 76 long axons in the subcortical white matter and calculated their equivalent circle radius $r = 0.9 \pm 0.2\,\mu\text{m}$ (Figure 4a), yielding the effective MR axon radius (1) $r_{\text{eff}} = 1.1 \pm 0.2\,\mu\text{m}$ and the coefficient of variation of the radius $\text{CV}(r) = 0.24 \pm 0.05$. Furthermore, we calculated the axonal skeleton and its undulation amplitude $w_0$ and wavelength $\lambda$ based on a single harmonic model, yielding $w_0 = 3.1 \pm 1.2\,\mu\text{m}$ and $\lambda = 28 \pm 10\,\mu\text{m}$. Finally, we calculated the correlation between the axon length, undulation amplitude, and wavelength (Figure 4b), showing that the axon length had low correlation with the undulation amplitude and wavelength, whereas the undulation amplitude and wavelength were highly correlated.

### 3.2 | Single-compartment SMT

The spherical mean of the MC-simulated signals of diffusion within human brain axons segmented from EM (Figure 2b) yielded a radius estimate $r_{\text{MR}} < 0.001\,\mu\text{m}$, much smaller than the histological $r_{\text{eff}} \approx 1.1\,\mu\text{m}$ (Figure 4a). This bias may arise from axonal undulations or caliber variations. To determine the most relevant features contributing to this bias, we translated the real axons from EM into artificial fibers of circular cross-sections with the same undulations and caliber variations, the simulated signals of which were almost the same as those of real axons (Figure 2b and Figure S2), and then scaled these features to generate artificial fibers with varying caliber variation and undulation amplitude (Figure 2a).

For the case without noise, the simulated spherical mean signals in the artificially generated fibers led to radius estimates $r_{\text{MR}}$ greater than the histological $r_{\text{eff}}$ (overestimation) in fibers with strong undulations, and radius estimates $r_{\text{MR}}$ smaller than the histological $r_{\text{eff}}$ (underestimation) in fibers with strong caliber variations (Figure 5a). The estimated axial diffusivity $D_a^{\parallel}$ decreased with undulations and caliber variations.

Simulations with added Rician noise (SNR = 100) showed that the axon diameter was generally underestimated due to the Rician noise floor, in cases of both undulations and caliber variations (Figure 5b). Furthermore, the precision was much lower due to the noise, which was manifested in the large values for NRMSE. In contrast, the estimated axial diffusivity decreased with undulations and caliber variations and was relatively unaffected by the noise.

In simulations and diameter mapping of individual axons (Figure 5), the estimated axial diffusivity $D_a^{\parallel}$ correlates well with the long-time prediction $D_{\infty,u}$ (13) due to undulations for axons with strong undulations (Figure 6a), though the correlation becomes weaker due to Rician noise at SNR = 100 (Figure 6b). Similarly, the estimated axial diffusivity $D_a^{\parallel}$ correlates with the long-time prediction $D_{\infty,\text{bead}}$ (14) due to beadings for axons with nontrivial caliber variations (Figure 6a), whereas this correlation is slightly weakened by Rician noise at SNR = 100 (Figure 6b).
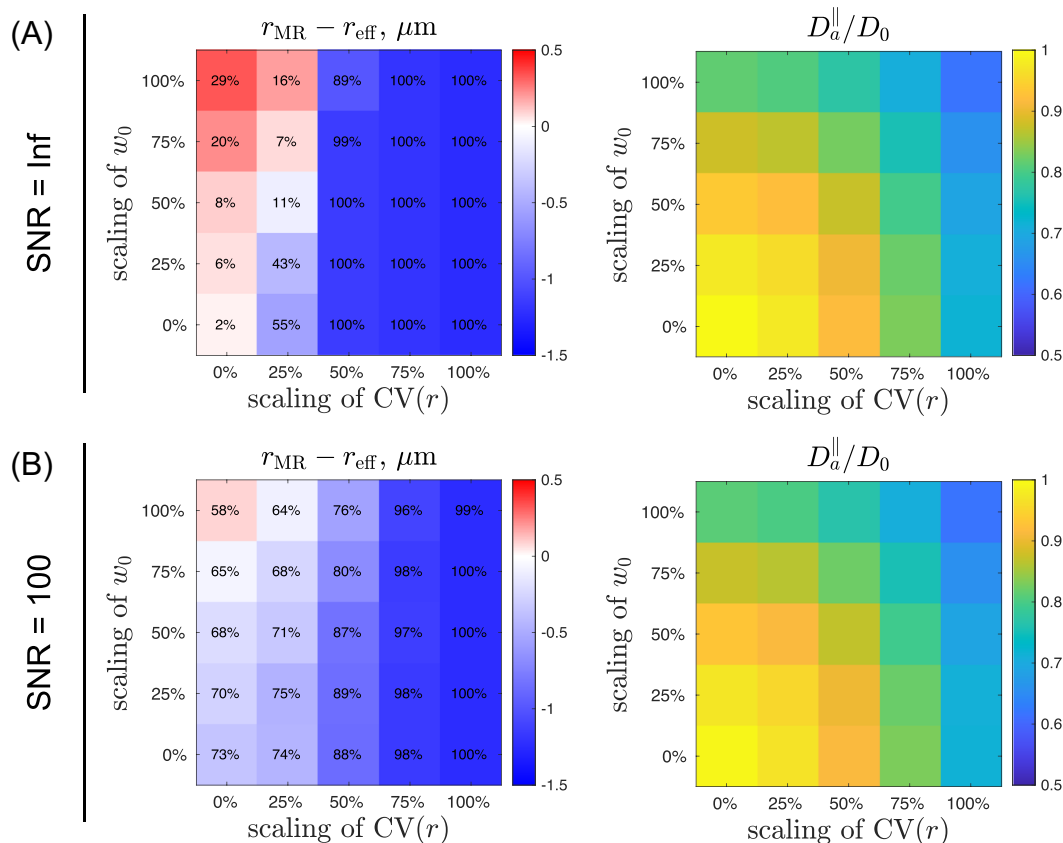
**FIGURE 5** Axon radius estimation based on diffusion simulations in undulating, beaded fibers reveals the effect of undulations and caliber variations on axonal diameter mapping, respectively. The single-compartment SMT model in Section 2.6.1 is fitted to intra-axonal signals in Section 2.5.1. The number in each pixel indicates the NRMSE between the estimation $r_{\mathrm{MR}}$ and histology $r_{\mathrm{eff}}$. When a parameter is underestimated, its NRMSE cannot exceed 100% due to the positive constraint in nonlinear least-squares fitting. (a) Simulations without adding noise show that undulations lead to overestimation of axon radius and caliber variations lead to underestimation of axon radius. Both undulations and caliber variations lead to a decrease in intra-axonal axial diffusivity. (b) Simulations with Rician noise (SNR = 100) show that a Rician noise floor leads to underestimation of axon radius in low precision, manifested by large NRMSE. The estimated intra-axonal axial diffusivity is relatively unaffected by the noise.

## 3.3 | Multicompartmental AxCaliber-SMT

To estimate the axon radius in white matter using diffusion data from all $b$ values, we combined the intra-axonal MC-simulated signals with axisymmetric Gaussian signals representing the extra-axonal space and isotropic Gaussian signals representing the CSF. We fitted the multicompartmental AxCaliber-SMT model in Equation (10) to the combined signals in Equation (3). The noiseless data led to overestimated axon radius in axons with strong undulations and underestimated axon radius in axons with strong caliber variations (Figures 7a, S3a, and S4a). In contrast, the combined signal with added Rician noise (SNR = 100) resulted in underestimated axon radius due to the Rician noise floor, for both undulations and caliber variations (Figures 7b, S3b, and S4b).

The biases in estimated volume fractions ($f_a$, $f_{\mathrm{csf}}$) and radial diffusivity in the extra-axonal space ($D_e^{\perp}$) were relatively unaffected by the Rician noise, though with slightly higher values of NRMSE (Figures 7, S3, and S4). The intra-axonal volume fraction was slightly underestimated in axons with strong undulations and overestimated in axons with strong caliber variations. The estimated CSF volume fraction and extra-axonal radial diffusivity were both overestimated while fixing $D_a^{\parallel} = D_e^{\parallel}$ at 1.2 or 1.7 $\mu m^2/ms$, for both undulations and caliber variations (Figures S3 and 7). In contrast, for $D_a^{\parallel} = D_e^{\parallel}$ fixed at 2 $\mu m^2/ms$, the estimated CSF volume fraction was underestimated for both undulations and caliber variations, whereas the extra-axonal radial diffusivity was under- and overestimated due to undulations and caliber variations, respectively (Figure S4).
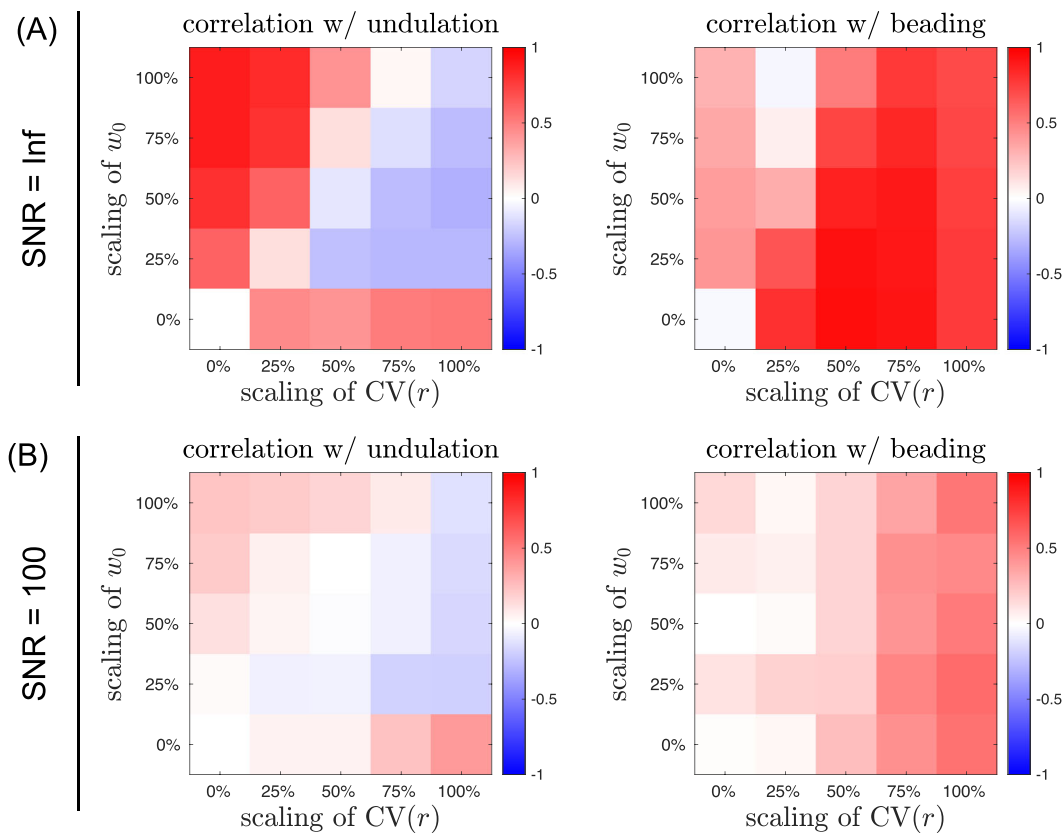
**FIGURE 6** Intra-axonal axial diffusivity estimation based on diffusion simulations in undulating, beaded fibers reveals its correlation with undulations and caliber variations, respectively. The single-compartment SMT model in Section 2.6.1 is fitted to intra-axonal signals in Section 2.5.1. The color indicates the Pearson correlation coefficient between the estimated $D_a^{\parallel}$ and the theoretical prediction due to undulations ($D_{\infty,u}$ in Equation 13) and caliber variations ($D_{\infty,\text{bead}}$ in Equation 14) in left and right panels, respectively. (a) Simulations without adding noise show that the prediction $D_{\infty,u}$ due to undulations correlates strongly with undulations, and the prediction $D_{\infty,\text{bead}}$ due to caliber variations correlates strongly with caliber variations. (b) Simulations with Rician noise (SNR = 100) show a similar trend in correlations with lower strength.

# 4 | DISCUSSION

In this work, we report the results of Monte Carlo simulations of diffusion inside axons segmented from EM images of human temporal subcortical white matter. Using the simulated diffusion signals, we study the performance of axonal diameter mapping using biophysical models of the diffusion MRI signal. To explore the effect of cellular-level features (i.e., undulations and beading) on MR estimates of axon diameter, we create fibers of circular cross-sections with varying scales of undulations and caliber variations based on those observed in the segmented axons and perform diffusion simulations in these fiber derivatives. Numerical simulations in three-dimensional EM-based microgeometries serve as a critical validation step for biophysical modeling of the diffusion MRI signal and provide important insights into the interpretation of quantitative biomarkers of axon diameter from diffusion MRI, particularly in fixed tissue, and their alterations in pathology.

## 4.1 | Single-compartment SMT

Axonal diameter mapping in white matter may be affected by strong undulations and caliber variations in axonal shape, as is observed in the fixed human brain tissue imaged here by EM. Caliber variations have previously been considered to be a major contributor to the overestimation of axon diameter, since the MR-measured effective radius in Equation (1) is heavily weighted by the tail (large axons) of the radius distribution[8,9,42]; however, our simulations show that caliber variations lead to underestimation of axon diameter in the actual model fitting to the spherical mean signals. The variation of local axial diffusivity and axial kurtosis along the length of individual axons may play a role in explaining this result (Section 4.2).

From a standard $q$-space analysis, a generic length scale of an ensemble-averaged diffusion propagator in the narrow pulse limit is given by[60]
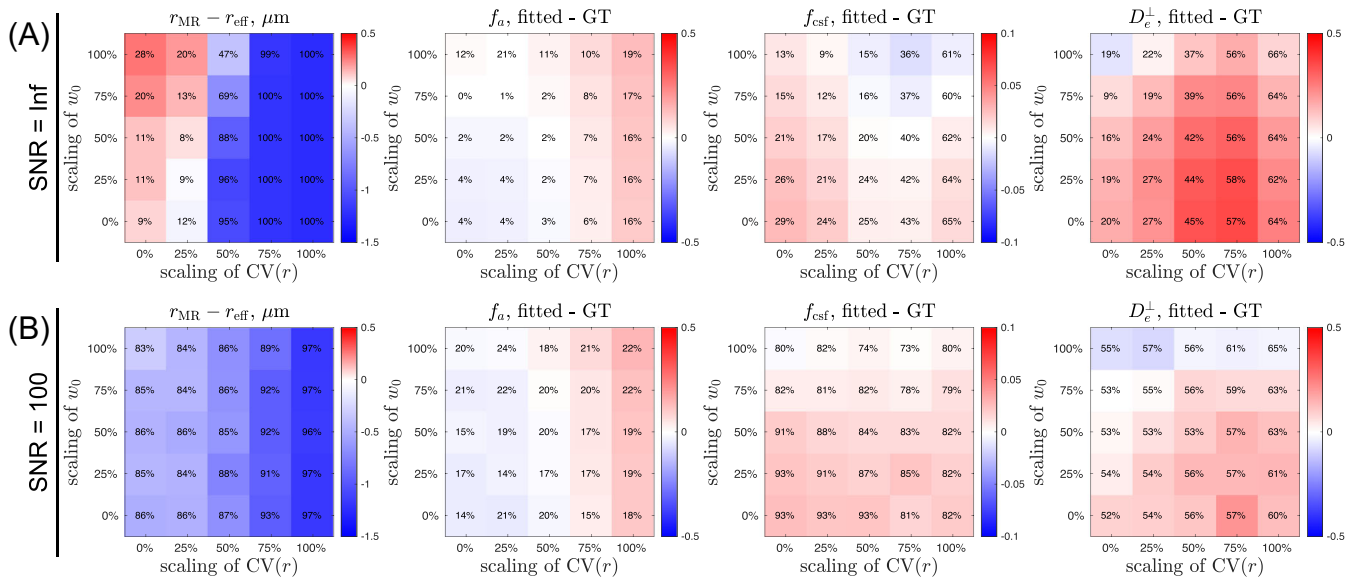
**FIGURE 7** Axon radius estimation based on diffusion simulations in undulating, beaded fibers reveals the effect of undulations and caliber variations on axonal diameter mapping, respectively. The multicompartmental AxCaliber-SMT model ($D_a^{\parallel} = D_e^{\parallel} = 1.7\,\mu m^2/ms$) in Section 2.6.2 is fitted to the multicompartmental signal in Section 2.5.2. The number in each pixel indicates the NRMSE between the estimation and ground truth. When a parameter is underestimated, its NRMSE cannot exceed 100% due to the positive constraint in nonlinear least-squares fitting. (a) Simulations without adding noise show that undulations lead to overestimation of axon radius and caliber variations lead to underestimation of axon radius. In contrast, the estimated intra-axonal volume fraction $f_a$ shows the opposite trend; undulations lead to slight underestimation of $f_a$ and caliber variations lead to overestimation of $f_a$. In addition, both undulations and caliber variations lead to overestimation of CSF volume fraction $f_{csf}$ and extra-axonal radial diffusivity $D_e^{\perp}$. (b) Simulations with Rician noise (SNR = 100) show that the Rician noise floor leads to underestimation of axon radius with low precision, manifested by large NRMSE. The bias in $f_a$, $f_{csf}$, and $D_e^{\perp}$ is similar to the noiseless result, and yet the precision is lower, that is, larger NRMSE. The radial diffusivity $D_e^{\perp}$ of the extra-axonal space is in units of $\mu m^2/ms$. GT = ground truth.

$$\frac{\pi}{q_{max}} = \pi\sqrt{\frac{t}{b_{max}}},$$

where $\pi/q_{max} \sim 2.8\,\mu m$ with diffusion time $t \simeq \Delta = 20\,ms$, and $b_{max} = 26\,ms/\mu m^2$ in this study. This length scale is associated with the $q$ dependence of the propagator in the *diffusion–diffraction regime*. However, it is not related to diffusion measurements of wide pulse sequence in thin fibers, where water molecules explore the axonal cross-section fully during the gradient pulse width; in this case, the diffusion phase has a narrow distribution due to the central limit theorem, leading to the *motion-narrowing regime*.[8,18]

For the case with added Rician noise (SNR = 100), the axon diameter is generally underestimated for axons with varying degrees of undulation and caliber variation. This can be understood based on an analysis of the resolution limit in axonal diameter mapping.[36,61] To evaluate the resolution limit, we first calculate the difference in the normalized spherical mean signals in Equation (7) between infinitely thin cylinders (sticks) and those with finite radius $r$:

$$\begin{aligned}\Delta S &= S(r)|_{r=0} - S(r) \\ &= [1 - \exp(-bD_a^{\perp})] \cdot h(A_a),\end{aligned} \tag{16}$$

with $h(\cdot)$ and $A_a$ defined in Equations (6) and (8). For thin fibers with radius $\sim 1\,\mu m$, the intra-axonal radial diffusivity is $D_a^{\perp} \sim 4.44 \times 10^{-4}\,\mu m^2/ms$ based on Neuman's solution (9) at $\delta = 10\,ms$, $\Delta = 20\,ms$, and $D_0 = 2\,\mu m^2/ms$. $D_a^{\perp}$ is much smaller than the intra-axonal axial diffusivity $D_a^{\parallel} \lesssim 2\,\mu m^2/ms$, justifying the approximation $D_a^{\parallel} \gg D_a^{\perp}$. Given the above estimation of $D_a^{\perp}$, we approximate $\exp(-bD_a^{\perp}) \simeq 1 - bD_a^{\perp}$ even at high $b$ values (e.g., up to $26\,ms/\mu m^2$ in this study), simplifying the analytical form of the signal difference further:

$$\Delta S \simeq bD_a^{\perp} \cdot h(A_a), \quad bD_a^{\perp} \ll 1. \tag{17}$$

To observe significantly different diffusion signals between zero-radius fibers and finite-radius ones, the $z$ score $z(\Delta S)$ of the signal difference is required to be larger than the $z$ threshold $z_\alpha$ for significance level $\alpha$[61]:

$$z(\Delta S) = \frac{\Delta S}{\sigma/\sqrt{n}} \geq z_\alpha, \tag{18}$$

where the noise level $\sigma$ is defined by the SNR $\equiv S_0/\sigma$ with $S_0 \equiv 1$, and the number $n$ of signal averages is the number of gradient directions per $b$ shell.

In the narrow pulse limit, the intra-axonal radial diffusivity is $D_a^\perp \simeq r^2/(4t)$. Substituting into Equations (17) and (18), we obtain the resolution limit of the axonal radius estimated using spherical mean signals of a narrow pulse sequence:

$$r \geq r_{\text{min, NP}} = \sqrt{\frac{4t\overline{\sigma}}{b}} \cdot h^{-1/2}(A_a), \tag{19}$$

where $\overline{\sigma} = z_\alpha/(\text{SNR}\sqrt{n})$. In the study, we have $D_a^\parallel \sim 1.7\,\mu\text{m}^2/\text{ms}$, maximal $b$ value $b = 26\,\text{ms}/\mu\text{m}^2$, $t \simeq \Delta = 20\,\text{ms}$, $n = 60$, and $z_\alpha = 1.64$ for $\alpha = 0.05$, yielding an estimate of the resolution limit $r_{\text{min,NP}} \sim 0.22\,\mu\text{m}$ at SNR = 100. Using a narrow pulse sequence, the resolution limit is much shorter than most of the axons. However, due to the limitations of gradient strength and slew rate on clinical and preclinical scanners, we performed axonal diameter mapping using diffusion measurements of a wide pulse sequence.

In the wide pulse limit (relevant for real experimental setups), substituting Equations (9) and (17) into Equation (18), we obtain the resolution limit for axonal diameter mapping using spherical mean signals[61]:

$$r \geq r_{\text{min}} = r_{\text{min}}^{(\text{par})} \cdot h^{-1/4}(A_a), \tag{20}$$

where $r_{\text{min}}^{(\text{par})}$ is the resolution limit for axonal diameter mapping by applying diffusion gradients transverse to highly aligned cylinders,

$$r_{\text{min}}^{(\text{par})} = \left( \frac{48}{7} \delta \left( \Delta - \frac{\delta}{3} \right) \frac{D_0\overline{\sigma}}{b} \right)^{1/4}, \tag{21}$$

and $\overline{\sigma} = z_\alpha/(\text{SNR}\sqrt{n})$. In the study, we have $D_0 = 2\,\mu\text{m}^2/\text{ms}$, $D_a^\parallel \sim 1.7\,\mu\text{m}^2/\text{ms}$, maximal $b$ value $b = 26\,\text{ms}/\mu\text{m}^2$, $\delta = 10\,\text{ms}$, $\Delta = 20\,\text{ms}$, $n = 60$, and $z_\alpha = 1.64$ for $\alpha = 0.05$, yielding estimates of $r_{\text{min}}^{(\text{par})} \sim 0.66\,\mu\text{m}$ and the resolution limit $r_{\text{min}} \sim 1.09\,\mu\text{m}$ at SNR = 100. The histological value $r_{\text{eff}} \sim 1.1\,\mu\text{m}$ (Figure 4a) is at the resolution limit $r_{\text{min}}$, explaining the high bias in axon radius estimation due to Rician noise in Figure 5b. For very thick axons (e.g., $r > 8\,\mu\text{m}$ for our sequence protocol), the values of $D_a^\parallel$ and $D_a^\perp$ are comparable and the resolution limit should be calculated by using the full functional form as in Andersson et al.[36] When diffusion signals are contributed by multiple compartments, the intra-axonal signal-to-noise ratio should be redefined as SNR $\equiv f_a S_0/\sigma$ with $f_a$ the intra-axonal volume fraction. This leads to even larger $\overline{\sigma}$ and subsequent increase of $r_{\text{min}}$, making it even harder to estimate the radius of thin axons.

In addition to the axon radius, the estimated axial diffusivity $D_a^\parallel$ decreases in axons with strong undulations and/or caliber variations. This is expected based on previous simulation studies: Budde and Frank[29] created fibers with periodic beads and showed that simulated axial diffusivity decreased with the strength of beading. Lee et al[20] performed diffusion simulations in realistic axonal shapes from mouse brain EM and showed that axial diffusivity decreased mainly due to caliber variations. Nilsson et al[30] and Lee et al[35] performed diffusion simulations in undulating fibers and showed the reduction of axial diffusivity due to undulations.

## 4.2 | Variation of local axial and radial diffusivities

Simulations in real axons and fibers mimicking realistic axons show that axon diameter is underestimated due to caliber variations. This finding is unexpected and cannot be explained by current axonal diameter mapping models. Here we suggest accounting for this observation by introducing the variation of local axial and radial diffusivities. It is challenging to consider the variation of local axial and radial diffusivities at the same time, let alone the local axial kurtosis (see the full functional form in C). Therefore, we discuss the two cases individually with an assumption of using specific distributions for local diffusivity and decide which case explains the observation better. For simplicity, we choose to use a Gamma distribution to explain the variation of local diffusivity $D$,[62]

$$\rho(D, \kappa, \theta) = \frac{D^{\kappa-1}}{\Gamma(\kappa)\theta^\kappa} \cdot \exp(-D/\theta), \tag{22}$$

where $\Gamma(\cdot)$ is Euler's Gamma function, $\kappa$ describes the shape, and $\theta$ describes the scale of the distribution. The mean and variance of diffusivity $D$ are $\kappa\theta$ and $\kappa\theta^2$, respectively.

### 4.2.1 | Variation of local radial diffusivity

In this case, we assume that local radial diffusivity varies along axons, whereas local axial diffusivity does not. The distribution of local radial diffusivity is described by a Gamma distribution $\rho(D_a^\perp, \kappa_\perp, \theta_\perp)$ in Equation (22). Given that the normalized spherical mean signal $S_a(b)$ in an axonal segment is given by Equation (7), the spherical mean signal summed over all axonal segments is

$$S(b, \kappa_\perp, \theta_\perp) = \int dD_a^\perp \, \rho(D_a^\perp, \kappa_\perp, \theta_\perp) \cdot \frac{r^2}{\langle r^2 \rangle_\rho} \cdot S_a(b), \tag{23}$$

where $\langle ... \rangle_\rho = \int dD_a^\perp \rho(D_a^\perp)...$, and the factor $r^2/\langle r^2 \rangle_\rho$ accounts for the volume fraction variation of each axonal cross-section. In the wide pulse limit, Neuman's solution (9) suggests $r^2 \propto \sqrt{D_a^\perp}$. Substituting into Equation (23), we obtain the spherical mean signal summed over all axonal segments,

$$S(b, \kappa_\perp, \theta_\perp) = h(A_a) \cdot (1 + b\theta_\perp)^{-(\kappa_\perp + \frac{1}{2})}. \tag{24}$$

We fit the above equation to the simulated spherical mean signal in real axons (Figure 8a) and obtain $\kappa_\perp < 0.001$, $\theta_\perp = 0.96\,\mu m^2/ms$, and $D_a^\| = 0.063\,\mu m^2/ms$, yielding an estimate of radius $< 0.001\,\mu m$. The estimated axial diffusivity and axon radius are both underestimated, with low quality of fit. Therefore, the variation of radial diffusivity fails to explain the observed underestimation of axon radius.

### 4.2.2 | Variation of local axial diffusivity

In this case, we assume that the local axial diffusivity varies along the length of the axons, and local radial diffusivity is kept constant along the axons. The distribution of local axial diffusivity is described by a Gamma distribution $\rho(D_a^\|, \kappa_\|, \theta_\|)$. Similarly, the spherical mean signal summed over all axonal segments is

$$S(b, \kappa_\|, \theta_\|) = \int dD_a^\| \rho(D_a^\|, \kappa_\|, \theta_\|) \cdot S_a(b).$$

Substituting Equations (7) and (22) into the above equation, we obtain[63]
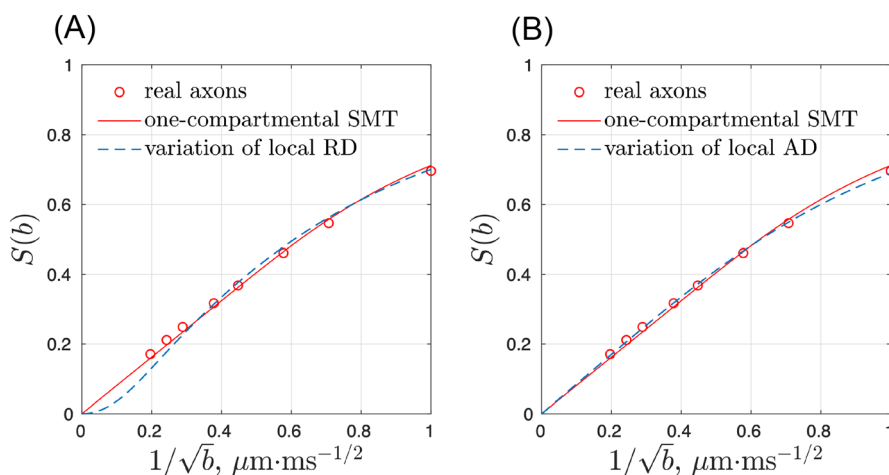


**FIGURE 8** To explain the underestimated axon radius due to caliber variations in Figure 5, we suggest accounting for this observation by using a Gamma distribution for variations of local diffusivity (a) transverse to or (b) parallel to axons in the intra-axonal signals (7). RD = radial diffusivity $D_a^\perp$, AD = axial diffusivity $D_a^\|$

$$S(b, \kappa_{\parallel}, \theta_{\parallel}) = {}_2F_1\left(\frac{1}{2}, \kappa_{\parallel}; \frac{3}{2}; -b\theta_{\parallel}\right) \cdot \exp(-bD_a^{\perp}), \tag{25}$$

where ${}_2F_1$ is a Gauss hypergeometric function. We fit the above functional form to the simulated spherical mean signals in real axons (Figure 8b) and obtain $\kappa_{\parallel} = 2.59$, $\theta_{\parallel} = 0.58\,\mu m^2/ms$, and an estimated radius $< 0.001\,\mu m$. This corresponds an estimate of $D_a^{\parallel} = 1.5 \pm 0.9\,\mu m^2/ms$. Though the estimated axon radius is much smaller than histological values using the $b$ value $\leq 26\,ms/\mu m^2$ (Figure 4a), the quality of fit for the Gamma-distributed $D_a^{\parallel}$ model (25) is better than that of the ordinary single-compartment SMT model (7). This better quality of fit shows the possibility of ADM in beaded axons using higher $b$ value and stronger gradient in the animal scanner and high-gradient human MR scanner in the future. The estimated mean and standard deviation of local axial diffusivity may thus serve as biomarkers that reflect properties of the underlying axonal beadings, as suggested in previous studies.[20,29]

This Gamma-distributed axial diffusivity leads to an additional contribution of axial kurtosis,[63]

$$K_a^{\parallel} = \frac{3\mathrm{var}(D_a^{\parallel})}{\langle D_a^{\parallel} \rangle^2} = \frac{3}{\kappa_{\parallel}}, \tag{26}$$

with an estimate of $K_a^{\parallel} \sim 1.16$ for the fit in Figure 8b. This axial kurtosis in human axons of this study is substantially higher than the axial kurtosis $\sim 0.44$ in mouse axons of Lee et al.[20] This is due to the stronger caliber variations and undulations in the human EM sample compared with the mouse EM sample. This may be caused by different fixation approaches, that is, immersion-fixed human sample versus perfusion-fixed mouse sample. Stronger axonal caliber variations and undulations lead to a wider distribution of local axial diffusivity, subsequently resulting in a higher overall axial kurtosis.

## 4.3 | Multicompartmental AxCaliber-SMT

In white matter, the diffusion signals receive contributions from multiple components, including intracellular water, extracellular water, and CSF. To estimate axon diameter using biophysical modeling of the dMRI signal, we consider signal contributions from all compartments for the full range of $b$ values.[14] To validate axonal diameter mapping models that account for multiple tissue compartments, we fit the multicompartmental AxCaliber-SMT model to the volume-weighted sum of simulated intra-axonal signals and anisotropic (extra-axonal space) and isotropic (CSF) Gaussian signals. Our simulations show that caliber variations lead to underestimated axon diameter, whereas undulations lead to overestimated axon diameter. These findings are similar to the results of the simulations and model fitting for the intra-axonal signals in isolation, as captured by the single-compartment SMT model. Considering the contribution of signals from multiple compartments does not significantly alter the results of axon diameter estimation.

Simulations with added Rician noise (SNR = 100) show that the axon diameter is underestimated for axons with either strong caliber variations or strong undulations. This observation can be explained by the resolution limit in Section 4.1.[36,61] It is worthwhile noting that the intra-axonal volume fraction $f_a$ varies around 0.75 (0.5–1) in simulations of multiple compartments, effectively resulting in a smaller SNR for intra-axonal signals. Therefore, in simulations of multiple compartments (Figure 7b), the bias due to noise is larger than that of the single-compartment SMT results (Figure 5b).

## 4.4 | Interpretation of alterations in axon diameter estimates

Axonal diameter mapping using the spherical mean dMRI signal is affected by the Rician noise floor and axonal morphology, including caliber variations and undulations. Our findings from systematic simulations in axonal substrates with varying caliber and undulations suggest that the interpretation of alterations in MR-estimated axon diameter should be performed with caution, especially in pathological tissues. For instance, the observation of decreased axon diameter could be the result of axonal beading and/or noise, whereas the observation of increased axon diameter could be the result of undulations.

The sensitivity of dMRI signals to caliber variations and undulations has been demonstrated in other works[29,33] and this study. Potential applications of these findings include monitoring axonal pathology, such as characterizing axonal undulations observed in human post-mortem brain tissue acutely following traumatic brain injury (TBI),[64] and axonal varicosity (beading) observed following multiple sclerosis,[65] TBI,[64,66] and ischemia in white matter.[67] Our findings suggest that axonal diameter mapping is potentially sensitive to axonal alterations, such as undulations in TBI patients and axonal beading in TBI and ischemic stroke patients.

## 4.5 | Limitations

The ex vivo human sample was fixed by immersion in paraformaldehyde and glutaraldehyde solution.[37] Undulations and caliber variations in the fixed tissue scanned with a serial sectioning EM may be stronger than in vivo, potentially due to fixation time for a large sample, shrinkage during tissue preparation, or even imperfect mechanical sectioning. In addition, the fixation method may be related to the undulation and caliber variation of white matter axons as well. For example, in previous studies,[22,43] the mouse brain EM samples were cardiac-perfusion fixed, and their white matter axons have relatively small undulations (amplitude $\sim$0.5 $\mu$m) and small caliber variations (CV($r$) $\sim$0.1). However, the human EM sample in this study was immersion-fixed, and the slower fixation process may lead to stronger undulations (amplitude $\sim$3 $\mu$m) and stronger caliber variations (CV($r$) $\sim$0.24). Therefore, the ex vivo human axons in this study may not be representative of in vivo healthy axons, but instead pathological ones.

Furthermore, the extra-axonal space signals are generated based on a time-independent Gaussian ellipsoid in our simulations. However, diffusion in the extra-axonal space is non-Gaussian; the diffusivity and kurtosis time dependence in the extra-axonal space are nontrivial and may contribute to biases in the estimation of axon diameter if the signal is dominated by low $b$ values.[8,17,18,68] Extra-cellular space maintenance strategies for immersion fixation[69] could be applied to preserve and image the extracellular space using EM in future studies. Further segmentation and diffusion simulation in extracellular space would help us to understand its contribution to the time dependence at low $b$ values.

Finally, in this work we have only considered axonal diameter mapping using the conventional pulsed-gradient spin-echo sequence, which is a linear tensor encoding scheme.[70] The effect of cellular-level features on axonal diameter mapping using other diffusion gradient waveforms,[71,72] such as planar and spherical tensor encoding waveforms, is not considered in this study. In Appendix D, we show that the resolution limit (smallest detectable axon radius) of the planar and spherical tensor encoding waveform is slightly smaller (i.e., better) than that of linear tensor encoding for a given $b$ value < 10 ms/$\mu$m$^2$ (planar tensor encoding) and < 5 ms/$\mu$m$^2$ (spherical tensor encoding). However, due to limitations in slew rate and echo time, generalized diffusion gradient waveforms aside from linear tensor encoding generally achieve much lower $b$ values than linear tensor encoding. It is difficult to distinguish intra-axonal and extra-axonal signals at low $b$ values, and thus using generalized waveforms is still less efficient than using linear tensor encoding for axonal diameter mapping. Alternatively, other advanced diffusion protocols using multiple time points,[4,5,16] diffusion modeling using higher order spherical harmonics,[73,74] or multiple contrast mechanisms ($T_2$, $T_2^*$, magnetization transfer) may help to resolve this complicated problem in axonal diameter mapping.

## 5 | CONCLUSIONS

Monte Carlo simulations of diffusion in realistic axonal substrates and their fiber derivatives show that axonal diameter mapping in white matter axons is affected by caliber variations and undulations, the two salient axonal features in fixed human brain tissue imaged by EM. Applying axonal diameter mapping on the simulated spherical mean signal demonstrates an underestimated axon diameter in axons with strong caliber variations and overestimated axon diameter in those with strong undulations. This finding suggests that the interpretation of alterations in MR-estimated axon caliber in studies of pathological white matter tissue should factor in caliber variations and undulations as potential contributors to observed decreases or increases in axon diameter, respectively. The relevance of these findings to in vivo axonal diameter mapping will require further exploration and systematic multimodality validation.

### ORCID
*Hong-Hsi Lee* https://orcid.org/0000-0002-3663-6559
*Qiyuan Tian* https://orcid.org/0000-0002-8350-5295
*Gabriel Ramos-Llorden* https://orcid.org/0000-0003-4020-705X
*Ali Abdollahzadeh* https://orcid.org/0000-0001-6234-2012
*Els Fieremans* https://orcid.org/0000-0002-1384-8591

*Dmitry S. Novikov* [ORCID] https://orcid.org/0000-0002-4213-3050

*Susie Y. Huang* [ORCID] https://orcid.org/0000-0003-2950-7254

## REFERENCES

1. Novikov DS, Fieremans E, Jespersen SN, Kiselev VG. Quantifying brain microstructure with diffusion MRI: Theory and parameter estimation. *NMR Biomed*. 2019;32:e3998.
2. Lovas G, Szilágyi N, Majtényi K, Palkovits M, Komoly S. Axonal changes in chronic demyelinated cervical spinal cord plaques. *Brain*. 2000;123(2): 308-317.
3. DeLuca GC, Ebers GC, Esiri MM. Axonal loss in multiple sclerosis: A pathological survey of the corticospinal and sensory tracts. *Brain*. 2004;127(5): 1009-1018.
4. Huang SY, Tobyne SM, Nummenmaa A, et al. Characterization of axonal disease in patients with multiple sclerosis using high-gradient-diffusion mr imaging. *Radiology*. 2016;280(1):244-251.
5. Huang SY, Tian Q, Fan Q, et al. High-gradient diffusion MRI reveals distinct estimates of axon diameter index within different white matter tracts in the in vivo human brain. *Brain Struct Funct*. 2020;225(4):1277-1291.
6. Cluskey S, Ramsden DB. Mechanisms of neurodegeneration in amyotrophic lateral sclerosis. *Molec Pathol*. 2001;54(6):386.
7. Tandan R, Bradley WG. Amyotrophic lateral sclerosis: Part 1. clinical features, pathology, and ethical issues in management. *Ann Neurol: Official J Am Neurolog Assoc Child Neurol Soc*. 1985;18(3):271-280.
8. Burcaw LM, Fieremans E, Novikov DS. Mesoscopic structure of neuronal tracts from time-dependent diffusion. *NeuroImage*. 2015;114:18-37.
9. Veraart J, Nunes D, Rudrapatna U, et al. Noninvasive quantification of axon radii using diffusion MRI. *eLife*. 2020;9:e49855.
10. Assaf Y, Blumenfeld-Katzir T, Yovel Y, Basser PJ. AxCaliber: A method for measuring axon diameter distribution from diffusion MRI. *Magnet Reson Med: Offic J Int Soc Magnet Reson Med*. 2008;59(6):1347-1354.
11. Barazany D, Basser PJ, Assaf Y. In vivo measurement of axon diameter distribution in the corpus callosum of rat brain. *Brain*. 2009;132(5):1210-1220.
12. Alexander DC, Hubbard PL, Hall MG, et al. Orientationally invariant indices of axon diameter and density from diffusion MRI. *NeuroImage*. 2010;52(4): 1374-1389.
13. Benjamini D, Komlosh ME, Holtzclaw LA, Nevo U, Basser PJ. White matter microstructure from nonparametric axon diameter distribution mapping. *NeuroImage*. 2016;135:333-344.
14. Fan Q, Nummenmaa A, Witzel T, et al. Axon diameter index estimation independent of fiber orientation distribution using high-gradient diffusion MRI. *Neuroimage*. 2020;222:117197.
15. Harkins KD, Beaulieu C, Xu J, Gore JC, Does MD. A simple estimate of axon size with diffusion MRI. *Neuroimage*. 2021;227:117619.
16. Warner W, Palombo M, Cruz R, et al. Temporal diffusion ratio (tdr) for imaging restricted diffusion: Optimisation and pre-clinical demonstration. *NeuroImage*. 2023;269:119930.
17. Fieremans E, Burcaw LM, Lee H-H, Lemberskiy G, Veraart J, Novikov DS. In vivo observation and biophysical interpretation of time-dependent diffusion in human white matter. *NeuroImage*. 2016;129:414-427.
18. Lee H-H, Fieremans E, Novikov DS. What dominates the time dependence of diffusion transverse to axons: Intra-or extra-axonal water? *NeuroImage*. 2018;182:500-510.
19. Novikov DS, Jensen JH, Helpern JA, Fieremans E. Revealing mesoscopic structural universality with diffusion. *Proc Nat Acad Sci United States Am*. 2014;111(14):5088-5093.
20. Lee H-H, Papaioannou A, Kim S-L, Novikov DS, Fieremans E. A time-dependent diffusion MRI signature of axon caliber variations and beading. *Commun Biol*. 2020;3(1):1-13.
21. Ronen I, Budde M, Ercan E, Annese J, Techawiboonwong A, Webb AG. Microstructural organization of axons in the human corpus callosum quantified by diffusion-weighted magnetic resonance spectroscopy of n-acetylaspartate and post-mortem histology. *Brain Struct Funct*. 2014;219(5):1773-1785.
22. Lee H-H, Yaros K, Veraart J, et al. Along-axon diameter variation and axonal orientation dispersion revealed with 3D electron microscopy: Implications for quantifying brain white matter microstructure with histology and diffusion MRI. *Brain Struct Funct*. 2019;224(4):1469-1488.
23. Grussu F, Schneider T, Yates RL, et al. A framework for optimal whole-sample histological quantification of neurite orientation dispersion in the human spinal cord. *J Neurosci Methods*. 2016;273:20-32.
24. Jespersen SN, Olesen JL, Hansen B, Shemesh N. Diffusion time dependence of microstructural parameters in fixed spinal cord. *NeuroImage*. 2018;182: 329-342.
25. Deoni SCL, Rutt BK, Arun T, Pierpaoli C, Jones DK. Gleaning multicomponent T1 and T2 information from steady-state imaging data. *Magnet Reson Med: Offic J Int Soc Magnet Reson Med*. 2008;60(6):1372-1387.
26. Lampinen B, Szczepankiewicz F, van Westen D, et al. Optimal experimental design for filter exchange imaging: Apparent exchange rate measurements in the healthy brain and in intracranial tumors. *Magnet Reson Med*. 2017;77(3):1104-1114.
27. Jespersen SN, Lundell H, Sønderby CK, Dyrby TB. Orientationally invariant metrics of apparent compartment eccentricity from double pulsed field gradient diffusion experiments. *NMR Biomed*. 2013;26(12):1647-1662.
28. Kaden E, Kelm ND, Carson RP, Does MD, Alexander DC. Multicompartment microscopic diffusion imaging. *NeuroImage*. 2016;139:346-359.
29. Budde MD, Frank JA. Neurite beading is sufficient to decrease the apparent diffusion coefficient after ischemic stroke. *Proc Nat Acad Sci*. 2010; 107(32):14472-14477.
30. Nilsson M, Lätt J, Ståhlberg F, van Westen D, Hagslätt H. The importance of axonal undulation in diffusion MR measurements: A Monte Carlo simulation study. *NMR Biomed*. 2012;25(5):795-805.
31. Neuman CH. Spin echo of spins diffusing in a bounded medium. *J Chem Phys*. 1974;60(11):4508-4511.
32. van Gelderen P, de Vleeschouwer MHM, DesPres D, Pekar J, van Zijl PCM, Moonen CTW. Water diffusion and acute stroke. *Magnet Reson Med*. 1994;31(2):154-163.
33. Brabec J, Lasič S, Nilsson M. Time-dependent diffusion in undulating thin fibers: Impact on axon diameter estimation. *NMR Biomed*. 2020;33(3):e4187.
34. Jeurissen B, Leemans A, Tournier J-D, Jones DK, Sijbers J. Investigating the prevalence of complex fiber configurations in white matter tissue with diffusion magnetic resonance imaging. *Human Brain Mapping*. 2013;34(11):2747-2766.

35. Lee H-H, Jespersen SN, Fieremans E, Novikov DS. The impact of realistic axonal shape on axon diameter estimation using diffusion MRI. *NeuroImage*. 2020;223:117228.

36. Andersson M, Pizzolato M, Kjer HM, Skodborg KF, Lundell H, Dyrby TB. Does powder averaging remove dispersion bias in diffusion MRI diameter estimates within real 3d axonal architectures? *NeuroImage*. 2022;248:118718.

37. Shapson-Coe A, Januszewski M, Berger DR, et al. A connectomic study of a petascale fragment of human cerebral cortex. *BioRxiv*. 2021. doi:10.1101/2021.05.29.446289

38. Tian Q, Ngamsombat C, Lee H-H, et al. Automated segmentation of human axon and myelin from electron microscopy data using deep learning for microstructural validation and simulation. In: Proc. Int. Soc. Magn. Reson. Med, Vol. 28; 2020:430.

39. Huang SY, Witzel T, Keil B, et al. Connectome 2.0: Developing the next-generation ultra-high gradient strength human MRI scanner for bridging studies of the micro-, meso-and macro-connectome. *NeuroImage*. 2021;243:118530.

40. West KL, Kelm ND, Carson RP, Does MD. A revised model for estimating g-ratio from MRI. *NeuroImage*. 2016;125:1155-1158.

41. Abdollahzadeh A, Belevich I, Jokitalo E, Tohka J, Sierra A. Automated 3D axonal morphometry of white matter. *Sci Rep*. 2019;9(1):6084.

42. Sepehrband F, Alexander DC, Kurniawan ND, Reutens DC, Yang Z. Towards higher sensitivity and stability of axon diameter estimation with diffusion-weighted MRI. *NMR Biomed*. 2016;29(3):293-308.

43. Lee H-H, Fieremans E, Novikov DS. Realistic microstructure simulator (rms): Monte carlo simulations of diffusion in three-dimensional cell segmentations of microscopy images. *J Neurosci Methods*. 2021;350:109018.

44. Fieremans E, Lee H-H. Physical and numerical phantoms for the validation of brain microstructural MRI: A cookbook. *NeuroImage*. 2018;182:39-61.

45. Dhital B, Reisert M, Kellner E, Kiselev VG. Intra-axonal diffusivity in brain white matter. *NeuroImage*. 2019;189:543-550.

46. Novikov DS, Veraart J, Jelescu IO, Fieremans E. Rotationally-invariant mapping of scalar and orientational metrics of neuronal microstructure with diffusion MRI. *NeuroImage*. 2018;174:518-538.

47. Veraart J, Fieremans E, Novikov DS. On the scaling behavior of water diffusion in human brain white matter. *NeuroImage*. 2019;185:379-387.

48. Howard AFD, Cottaar M, Drakesmith M, et al. Estimating axial diffusivity in the noddi model. *NeuroImage*. 2022;262:119535.

49. Callaghan PT, Jolley KW, Lelievre J. Diffusion of water in the endosperm tissue of wheat grains as studied by pulsed field gradient nuclear magnetic resonance. *Biophys J*. 1979;28(1):133-141.

50. Gudbjartsson H, Patz S. The Rician distribution of noisy MRI data. *Magnet Reson Med*. 1995;34(6):910-914.

51. Koay CG, Basser PJ. Analytically exact correction scheme for signal extraction from noisy magnitude MR signals. *J Magnet Reson*. 2006;179(2):317-322.

52. Jelescu IO, Veraart J, Fieremans E, Novikov DS. Degeneracy in model parameter estimation for multicompartmental diffusion in neuronal tissue. *NMR Biomed*. 2016;29(1):33-47.

53. Hellwig B, Schüz A, Aertsen A. Synapses on axon collaterals of pyramidal cells are spaced at random intervals: A golgi study in the mouse cerebral cortex. *Biolog Cybern*. 1994;71(1):1-12.

54. Glantz LA, Lewis DA. Decreased dendritic spine density on prefrontal cortical pyramidal neurons in schizophrenia. *Arch Gen Psych*. 2000;57(1):65-73.

55. Shepherd GMG, Raastad M, Andersen P. General and variable features of varicosity spacing along unmyelinated axons in the hippocampus and cerebellum. *Proc Nat Acad Sci*. 2002;99(9):6340-6345.

56. Morales J, Benavides-Piccione R, Dar M, et al. Random positions of dendritic spines in human cerebral cortex. *J Neurosci*. 2014;34(30):10078-10084.

57. Lee H-H, Papaioannou A, Novikov DS, Fieremans E. In vivo observation and biophysical interpretation of time-dependent diffusion in human cortical gray matter. *NeuroImage*. 2020;222:117054.

58. Novikov DS. The present and the future of microstructure MRI: From a paradigm shift to normal science. *J Neurosci Methods*. 2020;351:108947.

59. Abdollahzadeh A, Coronado-Leija R, Mehrin S, et al. Characterization of white matter myelinated and unmyelinated axons from diffusion MRI perspective, 31st Annual Meeting of the International Society for Magnetic Resonance in Medicine, Toronto, ON, Canada, Vol. 31; 2023:4322.

60. Callaghan PT. *Principles of nuclear magnetic resonance microscopy*: Oxford University Press on Demand; 1993.

61. Nilsson M, Lasič S, Drobnjak I, Topgaard D, Westin C-F. Resolution limit of cylinder diameter estimation by diffusion MRI: The impact of gradient waveform and orientation dispersion. *NMR Biomed*. 2017;30(7):e3711.

62. Jian B, Vemuri BC, Özarslan E, Carney PR, Mareci TH. A novel tensor distribution model for the diffusion-weighted mr signal. *NeuroImage*. 2007;37(1):164-176.

63. Jensen JH. Impact of intra-axonal kurtosis on fiber orientation density functions estimated with fiber ball imaging. *Magnet Reson Med*. 2022;88(3):1347-1354.

64. Tang-Schomer MD, Johnson VE, Baas PW, Stewart W, Smith DH. Partial interruption of axonal transport due to microtubule breakage accounts for the formation of periodic varicosities after traumatic axonal injury. *Experiment Neurol*. 2012;233(1):364-372.

65. Luchicchi A, Hart B, Frigerio I, et al. Axon-myelin unit blistering as early event in ms normal appearing white matter. *Ann Neurol*. 2021;89(4):711-725.

66. Johnson VE, Stewart W, Smith DH. Axonal pathology in traumatic brain injury. *Experimental Neurol*. 2013;246:35-43.

67. Garthwaite G, Brown G, Batchelor AM, Goodwin DA, Garthwaite J. Mechanisms of ischaemic damage to central white matter axons: a quantitative histological analysis using rat optic nerve. *Neurosci*. 1999;94(4):1219-1230.

68. De Santis S, Jones DK, Roebroeck A. Including diffusion time dependence in the extra-axonal space improves in vivo estimates of axonal diameter and density in human white matter. *NeuroImage*. 2016;130:91-103.

69. Karlupia N, Schalek RL, Wu Y, et al. Immersion fixation and staining of multicubic millimeter volumes for electron microscopy–based connectomics of human brain biopsies. *Biolog Psychiat*. 2023;96(4):352-360.

70. Stejskal EO, Tanner JE. Spin diffusion measurements: Spin echoes in the presence of a time-dependent field gradient. *J Chem Phys*. 1965;42(1):288-292.

71. Eriksson S, Lasič S, Nilsson M, Westin C-F, Topgaard D. NMR diffusion-encoding with axial symmetry and variable anisotropy: Distinguishing between prolate and oblate microscopic diffusion tensors with unknown orientation distribution. *J Chem Phys*. 2015;142(10):104201.

72. Westin C-F, Knutsson H, Pasternak O, Szczepankiewicz F, et al. Q-space trajectory imaging for multidimensional diffusion MRI of the human brain. *Neuroimage*. 2016;135:345-362.

73. Fan Q, Nummenmaa AA, Tian Q, Ohringer NA, Witzel T, et al. Investigating the benefits of incorporating higher order spherical harmonics in axon diameter measurements. In: 27th Annual Meeting of the International Society for Magnetic Resonance in Medicine, Montréal, QC, Canada, Vol. 27; 2019.

74. Veraart J, Raven EP, Jones DK, Palombo M. Axon diameter mapping is confounded by glial cells. In: Annual Meeting of the International Society for Magnetic Resonance in Medicine, Toronto, ON, Canada, Vol. 31; 2023:973.

75. Novikov DS, Kiselev VG. Effective medium theory of a diffusion-weighted signal. *NMR Biomed*. 2010;23(7):682-697.

76. Szczepankiewicz F, Westin C-F, Nilsson M. Maxwell-compensated design of asymmetric gradient waveforms for tensor-valued diffusion encoding. *Magnet Reson Medi*. 2019;82(4):1424-1437.

77. Fan Q, Eichner C, Afzali M, et al. Mapping the human connectome using diffusion MRI at 300 mT/m gradient strength: Methodological advances and scientific impact. *NeuroImage*. 2022;254:118958.

## SUPPORTING INFORMATION

Additional supporting information can be found online in the Supporting Information section at the end of this article.

## APPENDIX A: AXIAL DIFFUSIVITY TIME-DEPENDENCE DUE TO UNDULATIONS

For simplicity, we provide an approximate solution of axial diffusivity time dependence in a single harmonic undulating fiber with no caliber variations, perturbatively in $w_0/\lambda \ll 1$, compared with $w_0/\lambda \approx 0.11$ in real axons (Figure 4b). In the previous study,[35] we show that, in the narrow pulse limit, the axial diffusivity along an undulating fiber at diffusion time $t$ is given by

$$D_u(t) \equiv \frac{\langle z^2 \rangle}{2t} \simeq D_{\infty,u} + c_u \cdot \frac{1}{t}\left(1 - e^{-t/t_u^{\parallel}}\right),$$

where long-time diffusivity $D_{\infty,u}$, strength of diffusivity time dependence $c_u$, and correlation time $t_u^{\parallel}$ are defined as follows:

$$
\begin{aligned}
D_{\infty,u} &= \frac{D_0}{\xi^2}, \\
\xi &\simeq 1 + \sum_{m=1}^{\infty} \binom{\frac{1}{2}}{m}\binom{2m}{m} \cdot \left(\frac{w_0^2 k^2}{4}\right)^m \\
&\simeq 1 + \frac{1}{4}w_0^2 k^2, \, w_0 k \ll 1, \\
c_u &\simeq \frac{1}{128}w_0^4 k^2, \\
t_u^{\parallel} &= \frac{1}{4D_{\infty,u}k^2} \simeq \frac{1}{4D_0 k^2},
\end{aligned}
\tag{A1}
$$

with undulation amplitude $w_0$ and wavelength $\lambda$ ($k = 2\pi/\lambda$). The approximation $D_{\infty,u} \simeq D_0$ in Equation (A1), that is, $\xi \gtrsim 1$, is supported by the small value of $w_0 k \sim w_0/\lambda$ in real axons (Figure 4b).

Then it is straightforward to calculate the instantaneous diffusivity in $d = 1$ dimension along the fiber,

$$D_{\text{inst}}(t) \equiv \frac{1}{2}\partial_t \langle z^2 \rangle \simeq D_{\infty,u} + \frac{c_u}{t_u^{\parallel}} \cdot e^{-t/t_u^{\parallel}},$$

which yields the frequency $\omega$ dependent dispersive diffusivity in a standard way[1,8]:

$$\mathcal{D}_u(\omega) = -i\omega \int_0^{\infty} dt\, e^{i\omega t} D_{\text{inst}}(t) \tag{A2}$$

$$\simeq D_{\infty,u} + \frac{c_u}{t_u^{\parallel}} \cdot \frac{-i\omega t_u^{\parallel}}{1 - i\omega t_u^{\parallel}}. \tag{A3}$$

The knowledge of dispersive diffusivity enables us to evaluate the diffusion signal $S$ up to the second-order cumulant in any sequence:

$$-\ln S = \int \frac{d\omega}{2\pi} \mathcal{D}_u(\omega) |q_\omega|^2 + \mathcal{O}(g^4), \tag{A4}$$

where $q_\omega$ is the Fourier transform of the diffusion wave vector $q(t) = \int_0^t dt' g(t')$. For a pulsed-gradient sequence of interpulse time interval $\Delta$ and pulse width $\delta$, we have[8,60]

$$q_\omega = \frac{g}{(i\omega)^2} \left(e^{i\omega\delta} - 1\right)\left(e^{i\omega\Delta} - 1\right). \tag{A5}$$

Substituting Equations (A3) and (A5) into Equation (A4), we obtain the axial diffusivity $-\frac{1}{b}\ln S|_{b\to 0}$ measured by the wide pulsed-gradient sequence due to undulations:

$$D_u(t,\delta) \simeq D_{\infty,u} + \frac{c_u t_u^{\parallel 2}}{\delta^2(\Delta - \delta/3)} \cdot \left[2\frac{\delta}{t_u^{\parallel}} - 2 + 2e^{-\Delta/t_u^{\parallel}} + 2e^{-\delta/t_u^{\parallel}} - e^{-(\Delta-\delta)/t_u^{\parallel}} - e^{-(\Delta+\delta)/t_u^{\parallel}}\right] \tag{A6}$$

$$\simeq D_{\infty,u} + \frac{1}{256} \cdot \frac{w_0^4}{D_0\delta} \cdot \frac{1}{\Delta - \delta/3}, \delta \gg t_u^{\parallel}. \tag{A7}$$

In the wide pulse limit of undulations, that is, $\delta \gg t_u^{\parallel}$, the axial diffusivity due to undulations in Equation (A6) acquires the Neuman[31] form in Equation (A7). Interestingly, the wide pulse solution (A7) indicated that the diffusivity time dependence along an undulating fiber is mainly affected by the undulation amplitude $w_0 \sim 3\,\mu m$, but not the wavelength $\lambda \sim 30\,\mu m$. Furthermore, the diffusivity time dependence transverse and parallel to an undulating fiber (with no caliber variations) shows the same functional form, with different scales in long-time diffusivity (0 versus $D_{\infty,u}$), strength of diffusivity time dependence ($c_u^{\perp} = w_0^2/4$ versus $c_u^{\parallel} = c_u \sim w_0^4/\lambda^2$), and correlation time ($t_u^{\perp} = t_u$ versus $t_u^{\parallel} = t_u/4$).[35]

## APPENDIX B: AXIAL DIFFUSIVITY TIME DEPENDENCE DUE TO CALIBER VARIATIONS

Details in tissue microgeometry are homogenized by diffusion at long time, resulting in a coarse-grained effective medium with local varying diffusivity,[19,75] manifested by the power-law scaling in time-dependent instantaneous diffusivity[19]:

$$D_{\text{inst}}(t) \equiv \frac{1}{2}\partial_t \langle x^2 \rangle \simeq D_{\infty} + \mathcal{A} \cdot t^{-\vartheta} \tag{B1}$$

with long-time diffusivity $D_{\infty}$, strength of restrictions $\mathcal{A}$, and dynamical exponent $\vartheta = (p+d)/2$. The long-range density fluctuations of microstructure in $d$ dimensions is described by the structural exponent $p$ via its power spectrum. In the narrow pulse limit, the typical cumulant diffusion coefficient,

$$D(t) \equiv \frac{\langle x^2 \rangle}{2t} = \frac{1}{t}\int_0^t dt' D_{\text{inst}}(t'),$$

shows the same power-law scaling:

$$D(t) = D_{\infty} + c \cdot t^{-\vartheta}, c = \frac{\mathcal{A}}{1-\vartheta}, \vartheta < 1. \tag{B2}$$

Substituting Equation (B1) into Equation (A2) yields the frequency $\omega$ dependent dispersive diffusivity[19,57,75]:

$$\mathcal{D}(\omega) \simeq D_\infty + c \cdot (1-\vartheta) \cdot \Gamma(1-\vartheta) \cdot (-i\omega)^\vartheta, \tag{B3}$$

where $\Gamma(\cdot)$ is Euler's $\Gamma$ function. Further, substituting Equations (B3) and (A5) into Equation (A4), we obtain the general form of time-dependent diffusivity $-(1/b)\ln S|_{b\to 0}$ measured by using a wide pulsed-gradient sequence:

$$D(\Delta,\delta) \simeq D_\infty + \frac{\mathcal{A}}{\delta^2(\Delta-\delta/3)}[2f_\vartheta(\Delta) + 2f_\vartheta(\delta) - f_\vartheta(\Delta+\delta) - f_\vartheta(\Delta-\delta)], \vartheta \le 1, \tag{B4}$$

where

$$
\begin{aligned}
f_\vartheta(t) &= \int \frac{d\omega}{2\pi}\Gamma(1-\vartheta) \cdot (-i\omega)^{\vartheta-4} \cdot e^{-i\omega t} \\
&= \frac{1}{(\vartheta-1)(\vartheta-2)(\vartheta-3)} \cdot t^{3-\vartheta}.
\end{aligned}
$$

The relation $\Gamma(1-\vartheta) \cdot \Gamma(\vartheta) = \pi/\sin(\pi\vartheta)$ is applied to simplify the equation. We will use this generalized functional form to discuss the time-dependent axial diffusivity due to caliber variations.

## B.1 | Short-range disorder in one dimension: Axial diffusivity time dependence due to caliber variations

Diffusion along neurites is hindered by caliber variations, such as beadings and spines, the random arrangement of which along neurites in histology[53,54,56] indicates the short-range disorder in one dimension ($p=0$, $d=1$). This corresponds to a dynamical exponent $\vartheta=1/2$ and the diffusivity measured by using a wide pulsed-gradient sequence in Equation (B4):

$$
\begin{aligned}
D_{\text{bead}}(\Delta,\delta) &\simeq D_{\infty,\text{bead}} + \frac{4}{15} \cdot \frac{c_{\text{bead}}}{\delta^2(\Delta-\delta/3)} \cdot \left[-2\Delta^{5/2} - 2\delta^{5/2} + (\Delta+\delta)^{5/2} + (\Delta-\delta)^{5/2}\right] \\
&\simeq D_{\infty,\text{bead}} + c_{\text{bead}} \cdot \frac{\sqrt{\Delta}}{\Delta-\delta/3}\left[1 - \frac{8}{15}\sqrt{\frac{\delta}{\Delta}} - \frac{1}{48}\left(\frac{\delta}{\Delta}\right)^2\right], \frac{\delta}{\Delta} \ll 1,
\end{aligned}
\tag{B5}
$$

where $c_{\text{bead}} = 2\mathcal{A}$ is substituted based on Equation (B2), and the subscript "bead" denotes the caliber variation (beading). The above asymptotic behaviour in the $\delta/\Delta \ll 1$ limit actually works well for the wide-pulse case $\delta/\Delta \sim 1$ with an error <1% in diffusivity time dependence.

## APPENDIX C: THE EFFECT OF LOCAL AXIAL DIFFUSIVITY VARIATION ALONG AN INDIVIDUAL AXON ON AXONAL DIAMETER MAPPING

In Equation (7), axonal segments are assumed to be in cylindrical shape with the same local axial diffusivity $D_a^\parallel$ along each segment. However, the undulations and caliber variations along an individual axon lead to variations of local axial diffusivity in each axonal segment, that is, $D_a^\parallel(z)$ varying through the axon's main axis $z$. In addition, caliber variations $r(z)$ lead to variations of local radial diffusivity $D_a^\perp(z)$ in each axonal segment as well. The former effect was not considered in previous studies, and the latter one was approximated by the first-order expansion.[9] To account for these effects, the variation of local axial diffusivity and radial diffusivity in each axonal segment is considered in the calculation of the spherical mean signal:

$$S(b) = \int dz v(z) \cdot \psi(b,z), v(z) = \frac{\pi r^2(z)}{V},$$

where $dz v(z)$ and $V = \int dz v(z)$ are volumes of an axonal segment at $z$ and the whole axon, respectively. The spherical mean signal $\psi(b,z)$ of an axonal segment has the same functional form as in Equation (7), except that $D_a^\parallel(z)$ and $D_a^\perp(z)$ both vary in each segment. To estimate local diffusivity, $D_a^\parallel(z)$ and $D_a^\perp(z)$, along and transverse to axonal segments, it is necessary to perform MC simulations of diffusion with random walkers initialized in each axonal segment at $z$. It is very time-consuming to perform such simulations with reasonable precision of local diffusivity estimations.

In addition to local diffusivity, the variation of local axial kurtosis $K_a^\parallel(z)$ along an individual axon yields the next-order correction[47]:

$$\psi(b,z) \simeq e^{-bD_a^{\perp}} \int_0^1 d\zeta e^{-b(D_a^{\parallel}-D_a^{\perp})\zeta^2} \left[1 + \frac{K_a^{\parallel}}{6}\left(bD_a^{\parallel}\zeta^2\right)^2 + \mathcal{O}(b^3)\right], \zeta = \hat{g}\cdot\hat{n},$$

$$= \left[1 + \frac{K_a^{\parallel}\eta}{8}\right]\cdot e^{-bD_a^{\perp}}\cdot h(A_a) - \frac{K_a^{\parallel}\eta}{24}\left(2bD_a^{\parallel}+3\right)e^{-bD_a^{\parallel}}, \tag{C1}$$

where $\hat{g}$ and $\hat{n}$ are directions of the diffusion gradient and axon segment, and

$$\eta = \left(1 - \frac{D_a^{\perp}}{D_a^{\parallel}}\right)^{-2} \simeq 1, D_a^{\parallel} \gg D_a^{\perp}.$$

The second right-hand-side term in Equation (C1) decays much faster than the first term due to the exponential decay $\exp(-bD_a^{\parallel})$. Similarly, the local diffusivities $D_a^{\parallel}(z)$, $D_a^{\perp}(z)$ and local axial kurtosis $K_a^{\parallel}(z)$ have to be estimated by performing diffusion simulations with random walkers initialized in each axonal segment located at $z$.

## APPENDIX D: RESOLUTION LIMIT FOR AXONAL DIAMETER MAPPING USING GENERALIZED DIFFUSION GRADIENT WAVEFORM

For the generalized diffusion gradient waveform, the $q$-space trajectory imaging[72] can be described by a general **B** tensor. The diffusion-weighting tensor is given by

$$\mathbf{B} = \int_0^{\text{TE}} dt\, \mathbf{q}(t) \bigotimes \mathbf{q}^T(t),$$

where $\mathbf{q}(t) = \int_0^t dt'\, \mathbf{g}(t')$, and Larmor gradient $\mathbf{g}(t)$ is the product of the diffusion gradient and gyromagnetic ratio. For an axisymmetric **B** tensor, its axial and radial components, $b_{\parallel}$ and $b_{\perp}$, define its $b$ value (trace) $b = b_{\parallel} + 2b_{\perp}$ and anisotropy $b_{\Delta} = (b_{\parallel} - b_{\perp})/b \in \left[-\frac{1}{2}, 1\right]$. For conventional LTE, $b_{\Delta} = 1$; for STE, $b_{\Delta} = 0$; for PTE, $b_{\Delta} = -\frac{1}{2}$. Considering an axisymmetric signal kernel (i.e., cylinder in this case), the spherical mean signal measured by the axisymmetric **B**-tensor waveform is given by[71]

$$S(b,b_{\Delta}) = \exp\left(-bD_{\text{iso}} + \frac{A_a b_{\Delta}}{3}\right)\cdot h(A_a b_{\Delta}), \tag{D1}$$

where $D_{\text{iso}} = \frac{1}{3}(D_a^{\parallel} + 2D_a^{\perp})$, and $h(\cdot)$ and $A_a$ are defined in Equations (6) and (8). In the low-frequency limit, the frequency $\omega$ dependent dispersive diffusivity for restricted diffusion is $\text{Re}\mathcal{D}(\omega) \sim \omega^2$, and the radial diffusivity of a straight cylinder for an arbitrary gradient waveform can be approximated by[1,8,61]

$$D_a^{\perp} \simeq \frac{7}{96}\frac{r^4}{D_0}V_{\omega}, \tag{D2}$$

where $V_{\omega}$ is the spectral encoding variance defined from the second order of $\mathbf{q}(\omega)$ and is independent of the scaling of gradient strength:

$$V_{\omega} = \frac{1}{b}\int dt|\mathbf{g}(t)|^2, b = \int dt|\mathbf{q}(t)|^2.$$

In practice, the frequency spectrum of a general **B**-tensor waveform could be different in its $q_x$, $q_y$, and $q_z$ components. In Equation (D1), the $D_a^{\perp}$ is assumed to be similar when it is measured by $q_x$, $q_y$, $q_z$, and their vector combinations. Furthermore, the relation (D2) between $D_a^{\perp}$ and $r$ is approximated via the average of $D_a^{\perp}$ measured by applying $q_x$, $q_y$, and $q_z$, respectively. We will use the above relations to evaluate the resolution limit for axonal diameter mapping using axisymmetric **B**-tensor encoding sequences.

### D.1 | Resolution limit for axonal diameter mapping using STE and LTE spherical mean signal

To evaluate the resolution limit of axonal diameter mapping using a **B**-tensor encoding sequence with $b_\Delta \in [0,1]$, we calculate the difference of spherical mean signals (D1) between infinitely thin cylinders and those with finite radius (compare with Equation 16):

$$\Delta S(b_\Delta \geq 0) \simeq bD_a^\perp \left(\frac{2+b_\Delta}{3}\right) \cdot e^{-bD_a^\parallel(1-b_\Delta)/3} \cdot h(A_a b_\Delta),$$

where we approximate $\exp[-bD_a^\perp(2+b_\Delta)/3] \simeq 1 - bD_a^\perp(2+b_\Delta)/3$. Substituting $\Delta S(b_\Delta \geq 0)$ and $D_a^\perp$ in Equation (D2) into the requirement (18) of the resolution limit for axonal diameter mapping, we obtain

$$r_{\min}(\mathbf{B}) = r_{\min}^{(par)}(\mathbf{B}) \cdot \left(\frac{3}{2+b_\Delta} \frac{e^{bD_a^\parallel(1-b_\Delta)/3}}{h(A_a b_\Delta)}\right)^{1/4}, \, b_\Delta \geq 0, \tag{D3}$$

where $r_{\min}^{(par)}(\mathbf{B})$ is analogous to the resolution limit for axonal diameter mapping by applying a generalized LTE waveform (not just pulsed-gradient) of the same $V_\omega$ value transverse to highly aligned cylinders[61]:

$$r_{\min}^{(par)}(\mathbf{B}) = \left(\frac{96}{7} \frac{\overline{\sigma}D_0}{bV_\omega}\right)^{1/4}. \tag{D4}$$

Unlike LTE, the non-LTE waveform has an additional signal sensitivity to diffusion parallel to cylinders, even when the main axis of the **B**-tensor waveform is transverse to cylinders. This is manifested by the fact that $r_{\min}(\mathbf{B})$ is not the same as $r_{\min}^{(par)}(\mathbf{B})$ for the STE waveform ($b_\Delta = 0$):

$$r_{\min}(\mathbf{B}_{STE}) = r_{\min}^{(par)}(\mathbf{B}) \cdot \left(\frac{3}{2}e^{bD_a^\parallel/3}\right)^{1/4}, \tag{D5}$$

where $h(x) = 1$ for $x \to 0^+$ is applied.

For the LTE waveform ($b_\Delta = 1$), the resolution limit is given by

$$r_{\min}(\mathbf{B}_{LTE}) = r_{\min}^{(par)}(\mathbf{B}) \cdot h(A_a)^{-1/4}. \tag{D6}$$

Substituting $V_\omega = 2/\delta(\Delta - \delta/3)$ for the pulsed-gradient LTE into the above equation yields Equation (20).

### D.2 | Resolution limit for axonal diameter mapping using PTE spherical mean signal

To evaluate the resolution limit of axonal diameter mapping using a **B**-tensor encoding sequence with $b_\Delta \in [-\frac{1}{2}, 0)$, we calculate the difference of spherical mean signals (D1) between infinitely thin cylinders and those with finite radius (compare with Equation 16):

$$\Delta S(b_\Delta < 0) \simeq bD_a^\perp \cdot e^{-A_a(1-2|b_\Delta|)/3} \cdot h_i(A_a|b_\Delta|),$$

where we approximate $\exp(-bD_a^\perp) \simeq 1 - bD_a^\perp$, and

$$h_i(x) = \sqrt{\frac{\pi}{4} \frac{\mathrm{erfi}(\sqrt{x})}{\sqrt{x}}} \cdot e^{-x}.$$

Substituting $\Delta S(b_\Delta < 0)$ and $D_a^\perp$ in Equation (D2) into the requirement (18) of the resolution limit for axonal diameter mapping, we have

$$r_{\min}(\mathbf{B}) = r_{\min}^{(par)}(\mathbf{B}) \cdot \left(\frac{e^{A_a(1-2|b_\Delta|)/3}}{h_i(A_a|b_\Delta|)}\right)^{1/4}, \, b_\Delta < 0.$$

For a PTE waveform ($b_\Delta = -\frac{1}{2}$), the resolution limit for axonal diameter mapping is

$$r_{\min}(\mathbf{B}_{\text{PTE}}) = r_{\min}^{(\text{par})}(\mathbf{B}) \cdot h_i^{-1/4}(A_a/2)$$
$$\simeq r_{\min}^{(\text{par})}(\mathbf{B}) \cdot (bD_a^{\parallel})^{1/4}, \, bD_a^{\parallel} \gg 1, \tag{D7}$$

where $h_i(x) \simeq 1/(2x)$ for $x \gg 1$. Substituting Equation (D4) into the above equation, we notice that the resolution limit for the PTE waveform is independent of $b$ at high $b$ values,

$$r_{\min}(\mathbf{B}_{\text{PTE}}) \simeq \left(\frac{96}{7}\frac{\bar{\sigma}D_0 D_a^{\parallel}}{V_\omega}\right)^{1/4}, \, bD_a^{\parallel} \gg 1.$$

In other words, at high $b$ values, the resolution limit for the PTE waveform will not be significantly improved by applying stronger gradients.

We compare the resolution limit for axonal diameter mapping using LTE (D6), PTE (D7), and STE (D5) within total time $= 30$ ms for diffusion gradient application. The LTE waveform is initialized with a pulsed-gradient sequence of interpulse duration $\Delta = 20$ ms and pulse width $\delta = 10$ ms. The LTE, PTE, and STE are optimized and Maxwell-compensated based on a $b$-value maximizing framework,[76] where we set the maximal gradient strength and slew rate at 500 mT/m and 600 T/m/s to create the waveform, consistent with the spec of the Connectome 2.0 scanner.[39] Then we scale the diffusion gradient amplitude for a given $b$ value without applying constraints on maximal gradient strength and slew rate. The resolution limit is calculated for SNR $= 100$, $n = 60$, and $z_\alpha = 1.64$ for $\alpha = 0.05$. The intrinsic diffusivity and axial diffusivity are fixed at $D_0 = 2 \, \mu m^2/ms$ and $D_a^{\parallel} = 1.7 \, \mu m^2/ms$. For a given $b$ value, PTE and STE provide a slightly smaller (i.e., better) resolution limit than LTE for $b$ values $< 10$ ms/$\mu m^2$ and $< 5$ ms/$\mu m^2$, respectively (Figure D1). However, for a given maximal gradient strength (e.g., 300 mT/m for Connectome scanner 1.0[77]), PTE and STE can only achieve much smaller $b$ values, where the intra- and extra-axonal signals are difficult to distinguish. Therefore, LTE is still the most efficient waveform for axonal diameter mapping so far.
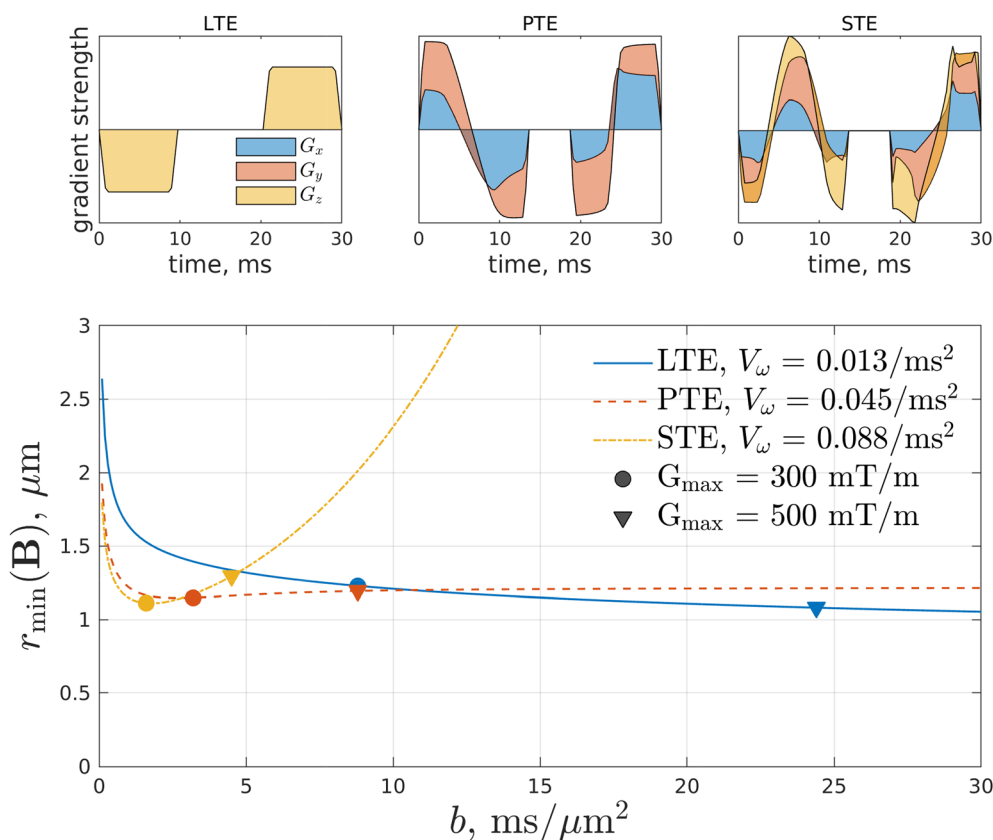


**FIGURE D1** Resolution limit, that is, smallest detectable axon radius $r_{\min}(\mathbf{B})$, for axonal diameter mapping using LTE (D6), PTE (D7), and STE (D5) waveforms. For a given $b$ value, PTE and STE lead to slightly smaller resolution limits than LTE for $b$ values $< 10$ ms/$\mu m^2$ and $< 5$ ms/$\mu m^2$, respectively. However, PTE and STE require much larger gradient strength to achieve the same $b$ values.